Lithospheric Origin of Oligocene–Miocene Magmatism in Central Chile: U–Pb Ages and Sr–Pb–Hf Isotope Composition of Minerals

P. MONTECINOS[1,2], U. SCHÄRER[1]*, M. VERGARA[2] AND L. AGUIRRE[2]

[1]UNIVERSITE DE NICE–SOPHIA ANTIPOLIS, GEOSCIENCES AZUR (UMR 6526), PARC VALROSE, F-06108 NICE, FRANCE
[2]UNIVERSIDAD DE CHILE, DEPARTAMENTO DE GEOLOGIA, PLAZA ERCILLA 803, CASILLA 13518, CORREO 21, SANTIAGO, CHILE

Establishing the petrogenesis of volcanic and plutonic rocks is a key issue in unraveling the evolution of distinct subduction-related tectonic phases occurring along the South American margin. This is particularly true for Cenozoic times when large volumes of magma were produced in the Andean belt. In this study we have focused on Oligo-Miocene magmatism in central Chile at 33°S. Our data include field and petrographic observations, whole-rock major and trace element analyses, U–Pb zircon dating, and Pb, Sr, and Hf isotope analyses of plagioclase, clinopyroxene, and zircon mineral separates. Combined with earlier dating results the new zircon ages define a 28·8–5·2 Ma period of plutonic and volcanic activity that ceased as a consequence of flattening subduction of the Nazca–Farallon plate. Rare earth elements patterns are variable, with up to 92 times chondrite concentrations for light rare earth elements yielding $(La/Yb)_N$ *between 3·6 and 7·0, and an absence of Eu anomalies. Initial Pb isotope signatures are in the range of 18·358–19·023 for* $^{206}Pb/^{204}Pb$*, 15·567–15·700 for* $^{207}Pb/^{204}Pb$ *and 38·249–39·084 for* $^{208}Pb/^{204}Pb$*. Initial* $^{87}Sr/^{86}Sr$ *are mostly in the range of 0·70369–0·70505, with two more radiogenic values at 0·7066. Initial Hf isotopic compositions of zircons yield exclusively positive* εHf_i *ranging between* $+6{\cdot}9$ *and* $+9{\cdot}6$*. The newly determined initial isotope characteristics of the Oligo-Miocene magmas suggest that the mantle source lithologies are different from both those of Pacific mid-ocean ridge basalt and ocean island basalt, plotting in the field of reference values for subcontinental lithospheric mantle, characterized by moderate large ion lithophile element–high field strengh element depletion and high* $^{238}U/^{204}Pb$*. A Hf model age of 2 Ga is estimated for the formation of the subcontinental mantle–continental crust assemblage in the region, suggesting that the initial Sr and Pb isotope ratios inferred for the source of the Oligo-Miocene parental magmas are the result of later Rb and U enrichment caused by mantle metasomatism. A time-integrated model Rb/Sr of* $\approx 0{\cdot}039$ *and* $\mu \approx 16$ *are estimated for the source of the parental magmas, consistent with ratios measured in peridotite xenoliths from continental areas. Evolution from predominant (>90%) basaltic–gabbroic to andesitic–dioritic magmas seems to involve a combination of (1) original trace element differences in the metasomatized subcontinental mantle, (2) different degrees of partial melting and (3) fractional crystallization in the garnet- and spinel-peridotite stability fields. The genesis of more differentiated magmas reaching rhyolitic–granitic compositions most probably also includes additional crystal fractionation at both shallow mantle depths and within the crust, possibly leading to some very minor assimilation of crustal material.*

KEY WORDS: *calc-alkaline magmatism; Oligo-Miocene; U–Pb dating; Sr–Pb–Hf isotopes; central Chile*

INTRODUCTION

Mesozoic and Cenozoic construction of the Andean belt is characterized by eastwards migration of magmatic arcs and crustal thickening, leading to the formation of high mountain chains generated during different tectonic phases and settings, related to varying plate configurations (e.g. Ramos, 2000). During Late Eocene and Early Oligocene times, subduction occurred at a rate of 6 cm/year, increasing to 15 cm/year during Late Oligocene and Early Miocene times. At ~20 Ma the roughly orthogonal

*Corresponding author. Telephone: +33-04-92-07-68-11. Fax: +33-04-92-07-68-16. E-mail: scharer@unice.fr

subduction direction rotated by about 10° in a northwards direction, associated with a decrease in convergence rate. This study is focused on the determination of the precise age and origin of Cenozoic volcanism and plutonism in the central part of the Andean belt at 33°S, where magmatism ceased about 5 Myr ago, associated with progressive flattening of the subducted slab (e.g. Ramos, 2000; Deckart *et al.*, 2005).

U–Pb zircon dating was undertaken to clarify ambiguities in the interpretation of earlier K–Ar and $^{40}Ar/^{39}Ar$ dates from the region, which are often affected by low-grade metamorphism and hydrothermal activity, both post-dating volcanic and plutonic rock emplacement. It is important to note that the rocks analyzed here were previously investigated by $^{40}Ar/^{39}Ar$ mineral dating (P. Montecinos, unpublished data), which revealed complex patterns from which no reliable ages could be derived.

Both zircon dating and isotope measurements were undertaken on fresh hand-picked minerals extracted from the least metamorphosed rocks, out of a series of 162 samples. U–Pb and Hf isotope analyses of zircon, and Pb and Sr isotopic analyses of feldspar and clinopyroxene were made on the same rocks. Some whole-rocks were also analyzed for major and trace elements. Because (1) these rocks are young, (2) Lu concentrations in zircon are extremely low, and (3) U and Rb concentrations are very low in plagioclase and clinopyroxene (e.g. Schärer, 1991; Schärer *et al.*, 1997), the measured isotopic ratios directly define the time-integrated initial ratios of the source lithologies at the time of melting.

GEOLOGICAL BACKGROUND

Figure 1a shows a schematic geological map of central Chile (33–36°S), two cross-sections, and a more detailed map of the study area (Fig. 1c) with sample locations. The Cenozoic volcanic–plutonic rocks form part of a north–south-oriented belt, trending parallel to the continental margin and extending over about 1300 km from 23 to 35°S (Nyström *et al.*, 2003). The thickness of the volcanic and plutonic units varies between about 2000 and 6000 m, constituting both the Principal and Frontal Cordilleras. Based on radiometric ages, these are subdivided into the Early Miocene Abanico Formation and the Middle to Late Miocene Farellones Formation (e.g. Nyström *et al.*, 2003; Kay *et al.*, 2005); however, this distinction is hampered by the fact that both formations contain similar lithologies. All the rock types contain secondary minerals such as prehnite, pumpellyite, actinolite, chlorite, sericite, calcite, zeolite, and epidote, produced during non-deformational low-grade metamorphism and fluid circulation (Levi *et al.*, 1989; Aguirre *et al.*, 2000). Tectonic activity associated with the emplacement of earlier Oligocene magmatic rocks was extensional, whereas subsequent activity during Miocene times changed to a compressional regime, reflecting convergence rates increasing from 6 to 15 cm/year (Charrier *et al.*, 2002; Kay *et al.*, 2005).

The Abanico and Farellones Formations comprise basalts, basaltic andesites, and andesites, and some more differentiated dacites and rhyolites (Nyström *et al.*, 2003; Kay *et al.*, 2005). Corresponding plutonic bodies range from gabbro to diorites, granodiorites and minor granites. Associated minor lithologies are pyroclastic flows and breccias, tuffs, and rhyolitic ashes. Basalts–gabbros and andesites–diorites are by far the most abundant lithologies, making up at least 90% of the magmatic rocks along the belt. There seems to be an evolutionary trend from the lower to the upper part of the series, with 80% basalts and 20% andesites in the basal part and 75% andesites, 20% basalts, and 5% dacites in the upper part. Intrusion of the largest (~15 km wide) granodioritic stocks into the andesites has produced up to 3 km wide epidote–actinolite–hornblende contact metamorphic aureoles.

Major and trace element geochemistry

The calc-alkaline character of the rocks composing the Oligo-Miocene magmatic belt has been documented in a series of studies (Fig. 2; Vergara *et al.*, 1988; Nyström *et al.*, 2003; Kay *et al.*, 2005; Muñoz *et al.*, 2006). They contain between 46·2 and 74·5 wt% SiO_2, correlating with the observed lithological variations of the volcanic and plutonic members, and have $(La/Yb)_N$ ratios between three and 16. Plagioclase fractionation in a few lithologies is suggested by Eu anomalies reaching $Eu/Eu^* = 0{\cdot}71$. Heavy rare earth element (HREE) concentrations are between eight and 20 times chondrite. In total alkali–silica (TAS) and AFM diagrams (Fig. 2) the rocks follow the typical differentiation trend of medium-K calc-alkaline magmas. Nyström *et al.* (2003) concluded that magmas of the apparently older Abanico Fm. were formed at shallower mantle depths than those of the Farellones Fm., with the Abanico parental magmas having segregated in the spinel peridotite stability field, whereas the younger Farellones mafic magmas show evidence of residual garnet in their source. Based on trace element ratios (e.g. Th/Yb vs Ta/Yb, Ta/Yb vs Ba/Th, Ba/La vs La/Yb) a minor contribution of minor crustal material was suggested, possibly including sediments (Nyström *et al.*, 2003; Deckart & Godoy, 2006).

Geochronology

K–Ar whole-rock dating of the Abanico and Farellones volcanic rocks (Fig. 1) has yielded ages between 20 and 4·1 Ma (Drake *et al.*, 1976; Vergara & Drake, 1979; Munizaga & Vicente, 1982; Beccar *et al.*, 1986; Vergara *et al.*, 1988). Roughly 100 km to the south, whole-rock K–Ar ages lie between 27·7 and 6·0 Ma (Kay *et al.*, 2005). Granitoid intrusions into these volcanic rocks yield K–Ar whole-rock ages ranging from 19·5 to 18·5 Ma

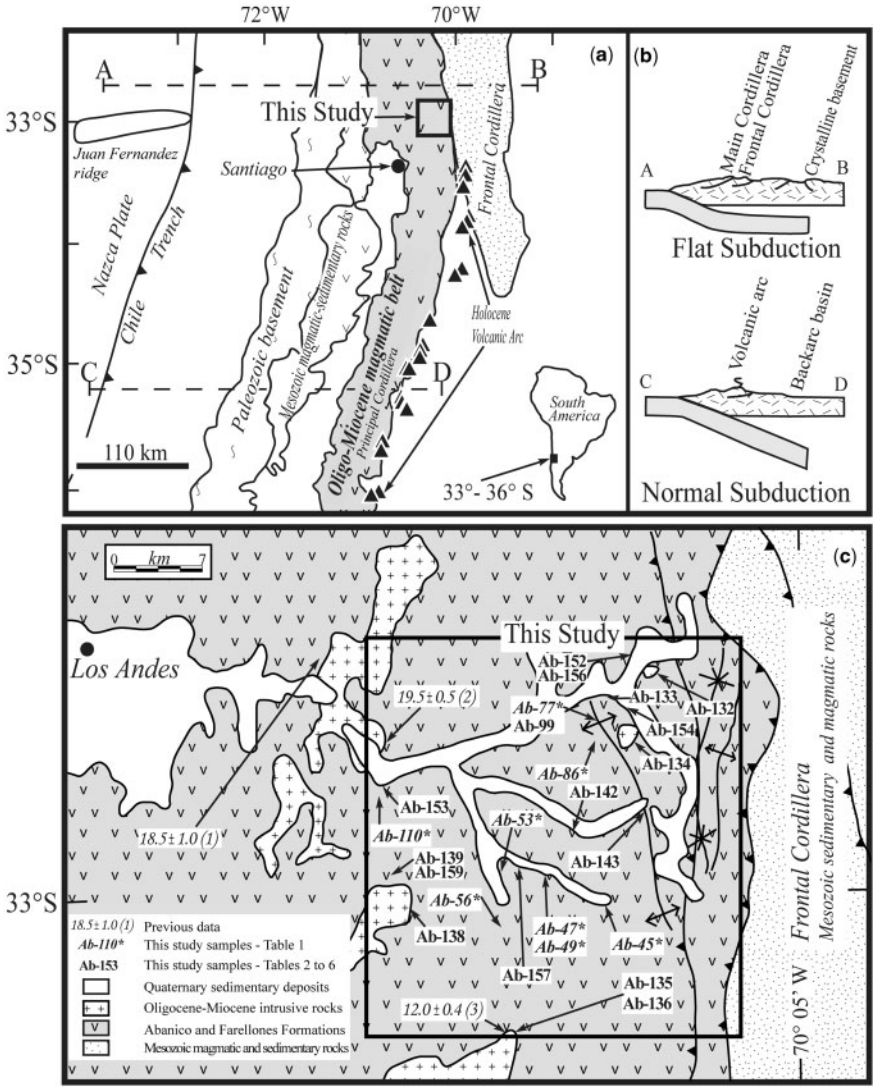

Fig. 1. (a) Schematic geological map of central Chile indicating the location of the Oligo-Miocene magmatic belt (Principal Cordillera) composed of the Abanico and Farellones formations. The map also shows all other major units such as the Paleozoic basement along the Pacific coast, the Mesozoic rocks, and the Frontal Cordillera. (b) Cross-sections to illustrate the present-day difference in subduction angles between latitudes 33° and 35°S (after Kay *et al.*, 2005). (c) Sample localities for rocks dated in this study using the U–Pb chronometer. Previously published ages (1–3) are by K–Ar on whole-rocks (Vergara & Drake, 1979; Munizaga & Vicente, 1982) and U–Pb on zircon (Deckart *et al.*, 2005).

(Munizaga & Vicente, 1982). Moreover, amphibole and biotite $^{40}Ar/^{39}Ar$ dates from the volcanic rocks give ages ranging from 28·8 to 18·6 Ma (Aguirre *et al.*, 2000; Fuentes *et al.*, 2002) and 50 km to the south, plagioclases from porphyritic basalts were dated at 34–18 Ma (Muñoz *et al.*, 2006). Amphibole and biotite $^{40}Ar/^{39}Ar$ ages of a granitoid intrusion a further 100 km to the south are 21·6 and 5·5 Ma (Kurtz *et al.*, 1997). Close to our study area, U–Pb dating of zircon has yielded ages of 17·2 and 16·8 Ma for two andesitic flows, 12·0 and 8·4 Ma for two intruding granodiorites, and 6·3–5·2 Ma for four porphyric dacitic rocks (Deckart *et al.*, 2005). Further U–Pb ages on zircons from two granodiorites about 50 km to the south yield ages of 11·3 and 10·3 Ma (Deckart & Godoy, 2006).

Sr–Nd–Pb isotope geochemistry

The petrogenesis of the Oligo-Miocene volcanic–plutonic series was previously addressed through major and trace element and Pb–Sr–Nd isotope measurements on whole-rock samples (Vergara *et al.*, 1999; Nyström *et al.*, 2003; Kay *et al.*, 2005; Muñoz *et al.*, 2006). The resulting models for the magmatism implicate varying mantle source regions and depths of magma generation (Nyström *et al.*, 2003; Kay *et al.*, 2005). Moreover, some basalts and andesites with ages of 20–18 Ma were interpreted to be

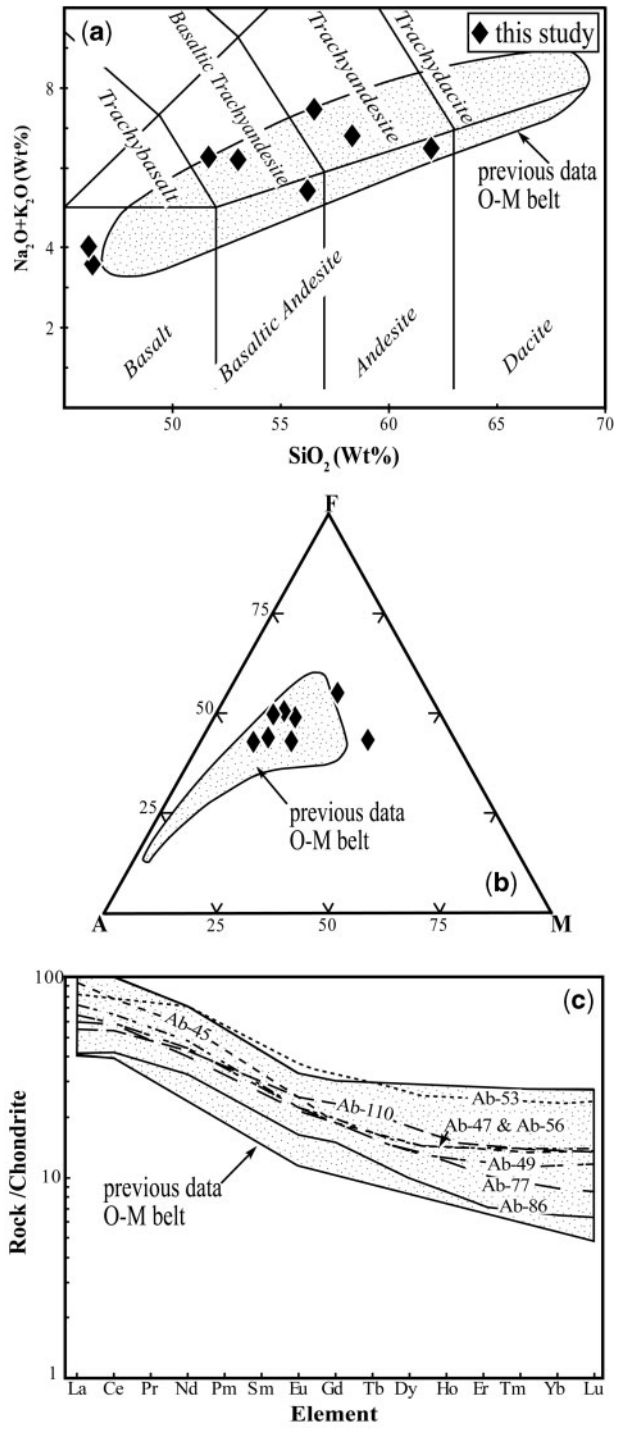

Fig. 2. Geochemical variations within the Oligo-Miocene magmatic belt. (a) Total alkalis vs SiO_2 (wt %) after Le Bas *et al.* (1986). (b) AFM diagram; A is total alkalis, F is total iron, and M is magnesium (all in wt %). (c) Chondrite-normalized REE patterns. Ab samples are the new samples from this study compared with the field of previously published data for the Oligo-Miocene (O-M) magmatic belt.

generated by the interaction of mantle-derived magmas with the lower continental crust (e.g. Kay *et al.*, 2005).

Data fields for these earlier data are shown for reference in the Figs 7–11 (summarized in Table 7). Initial $^{87}Sr/^{86}Sr$ ratios for both extrusive and intrusive lithologies lie in a very narrow range between 0·7033 and 0·7044 (Vergara *et al.*, 1999; Nyström *et al.*, 2003; Kay *et al.*, 2005; Deckart & Godoy, 2006; Muñoz *et al.*, 2006). For the same series of whole-rock samples from central Chile (33–36°S) initial epsilon Nd values (εNd_i) define a relatively narrow range between +3·0 and +6·2. Similarly homogeneous isotope characteristics are also observed for initial Pb ratios, yielding 18·453–18·588 for $^{206}Pb/^{204}Pb$, 15·548–15·610 for $^{207}Pb/^{204}Pb$, and 38·210–38·478 for $^{208}Pb/^{204}Pb$ (Vergara *et al.*, 1999; Nyström *et al.*, 2003; Kay *et al.*, 2005). For zircon of two granodioritic intrusions initial epsilon Hf values (εHf_i) lie at +4 and +8 (Deckart & Godoy, 2006).

Based on εNd_i vs initial $^{87}Sr/^{86}Sr$ isotopic ratios (Sr_i) Nyström *et al.* (2003) suggested a mantle source enriched in large ion lithophile elements (LILE) and high field strength elements (HFSE) compared with asthenospheric mantle. Moreover, Deckart & Godoy (2006) used εNd_i vs εHf to propose mixing between such enriched mantle and pelagic sediments; however, Kay *et al.* (2005) showed that εNd_i is independent of SiO_2, ruling out significant crustal contamination. Apart from petrological arguments suggesting increasingly deeper mantle melting with time (Nyström *et al.*, 2003) a correlated change from more to less LILE/HFSE depleted mantle sources was suggested (Kay *et al.*, 2005).

ANALYTICAL METHODS

Major and trace element analyses were performed by inductively coupled plasma atomicc emission spectrometry (ICP-AES) using a Perkin Elmer P400 instrument at the Geology Department of the University of Chile. Mineral compositions were determined on carbon-coated polished thin-sections using the wavelength-dispersive spectrometry (WDS) system of a CAMECA SX100 electron microprobe at the University of Montpellier II, France, calibrated with natural and synthetic standards. Results are considered to be accurate to within 1–3% for major elements. Mineral separation was carried out using a Frantz isodynamic magnetic separator, heavy liquids ($CHBr_3$ and CH_2I_2), and hand-picking under a binocular microscope. All U–Pb, Pb and Sr isotope analyses were performed at the University of Nice–Sophia Antipolis.

Initial Pb isotopic compositions were measured for primary magmatic feldspar. These data were also used to correct for common Pb in zircon as well as in the determination of $^{238}U/^{204}Pb$–$^{206}Pb/^{204}Pb$ isochron ages. Overall analytical uncertainties (2σ-STERR) for the U–Pb dates

are 2–4% for $^{206}Pb/^{238}U$, and 3–10% for $^{207}Pb/^{235}U$, including in-run precision and correction for blanks, mass-fractionation and common Pb. Lead blanks are 13–17 pg per analysis, with 5–7 pg coming from the PTFE® capsules and 8–10 pg from the chemical reagents. Typical ratios of sample to blank Pb lie around 10. Error ellipses in Figs 3–5 correspond to the above uncertainties with correlation coefficients between about 0·3 and 0·5. Analytical uncertainties are much smaller for the isochron data (no common Pb correction) at 0·10–2·0% for $^{206}Pb/^{204}Pb$ and 0·30–3·0% for $^{238}U/^{204}Pb$ (Table 3).

Prior to dissolution of zircon in >50% HF at 215°C for 3 days in PTFE® Teflon bombs, the solutions were spiked with a mixed $^{205}Pb/^{235}U/^{233}U$ solution, followed by the separation of U and Pb from Zr and Hf (Krogh, 1973). To eliminate ^{176}Yb interferences on ^{176}Hf, a separation step on AGW-50X cation resin® was used (Patchett & Tatsumoto, 1980). Hafnium isotope measurements were performed on a Nu plasma 1700 instrument at the Ecole Normale Supérieure at Lyon using the JMC-475 Hf standard for calibration, run every fourth sample (Blichert-Toft *et al.*, 1997). Hafnium isotope measurements were normalized to $^{179}Hf/^{177}Hf = 0·7325$ (Patchett & Tatsumoto, 1980). The chemical procedures for the combined U–Pb–Hf analyses of zircon have been described elsewhere (Bodet & Schärer, 2000).

Hand-picked feldspars and clinopyroxenes were washed in 6N HCl, ground in an agate mortar and leached with 1% HF/HBr 1N for a few minutes in an ultrasonic bath (see Schärer, 1991). Dissolution was performed in >50% HF overnight at 120°C in 2 ml Savilex beakers®. To confirm the low U abundance in these minerals, some analyses were spiked with the same ^{233}U–^{235}U–^{205}Pb solution as the zircons. For feldspar and clinopyroxene, a modified HBr procedure (Manhès *et al.*, 1978) was used to separate and purify Pb and U from major elements and Sr, followed by Sr separation from major elements and Rb using Eichrom Sr-Spec. resin®.

All U–Pb and Pb isotope analyses were carried out on single Re filaments (H_3PO_4/Si-gel load) using a single secondary electron multiplier on a Thomson 206 mass spectrometer. Mass-fractionation of 0·10 ± 0·05%/a.m.u. was controlled by repeated analyses of the NBS-981 standard, which yielded average ratios of 16·941 ± 0·004 (2σ-STERR) for $^{206}Pb/^{204}Pb$, 15·501 ± 0·004 for $^{207}Pb/^{204}Pb$, and 36·728 ± 0·009 for $^{208}Pb/^{204}Pb$. For concordia and isochron plots, and linear regression calculations we used the program ISOPLOT-3 (Ludwig, 2003).

Strontium isotopic compositions were measured on a VG-Sector instrument using single Re filaments with a H_3PO_4/TaF_5 load. The NBS-987 standard was regularly run to control the accuracy of Sr measurement yielding an average $(^{87}Sr/^{86}Sr)_{norm}$ of 0·702912 ± 0·000015 (2σ-STERR). All Sr isotope measurements were normalized to $^{86}Sr/^{88}Sr = 0·1194$.

RESULTS

The samples

A series of thin-sections from 162 rocks were studied to select samples with minimum metamorphic overprint, with well-preserved primary magmatic mineral assemblages. Sixteen samples of fresh plagioclase and clinopyroxene were chosen for Pb–Sr analysis. Eight rocks were chosen for U–Pb zircon dating, from which 13 zircon populations were selected for Hf isotope measurements. Eight whole-rocks were characterized for major and trace element and mineral compositions.

The samples analyzed are as follows.

(1) An olivine-phyric basalt (Ab-99) with a glomeroporphyritic texture containing between 5 and 20% euhedral to subhedral 1–2 mm olivine crystals. Augite crystals are 1–3 mm in size (2–5 vol.%,) and plagioclase ($An_{88–92}$) 1–5 mm (10–40 vol.%). The groundmass is composed of very small grains (<0·2 mm) of plagioclase, clinopyroxene and minor olivine. A chlorite–epidote–calcite assemblage represents altered augite.

(2) A gabbro sill (Ab-142) with a few per cent of 1–2 mm fresh augite and rare pigeonite, less than 2% olivine, and 30–50% fresh 1–4 mm plagioclase ($An_{72–86}$). The groundmass is composed of altered glass with clinopyroxene and plagioclase crystals ~0·1 mm in size. Apatite is an accessory mineral. Secondary minerals are calcite and chlorite in some augites, and phengite–sericite in the most altered plagioclase crystals.

(3) Three samples (Ab-154, -156, -159) were collected from different clinopyroxene-carrying andesitic flows, also characterized by glomero-porphyric textures. They are composed of fresh to intensely altered andesine ($An_{45–49}$) and glomerocrysts of augite ($Wo_{39}En_{39}Fs_{18}$ to $Wo_{40}En_{42}Fs_{21}$) in a groundmass of altered glass, locally showing pilotaxitic plagioclase. Micro-phenocrysts (<0·2 mm) of clinopyroxene and plagioclase also occur in the groundmass. Calcite, smectite and albite are secondary phases occurring in the most altered domains of the andesine phenocrysts. Epidote, calcite, and chlorite are secondary minerals formed after clinopyroxene.

(4) Two dacitic sills (Ab-133, -143) and an andesitic sill (Ab-152) were sampled from within the volcanic sequence. They exhibit porphyritic textures, composed of plagioclase phenocrysts (1·5–3 mm) in a groundmass of fine-grained feldspar and minor quartz. The dacitic sills contain primary phenocrystic muscovite (0·5–2 mm) and altered amphibole

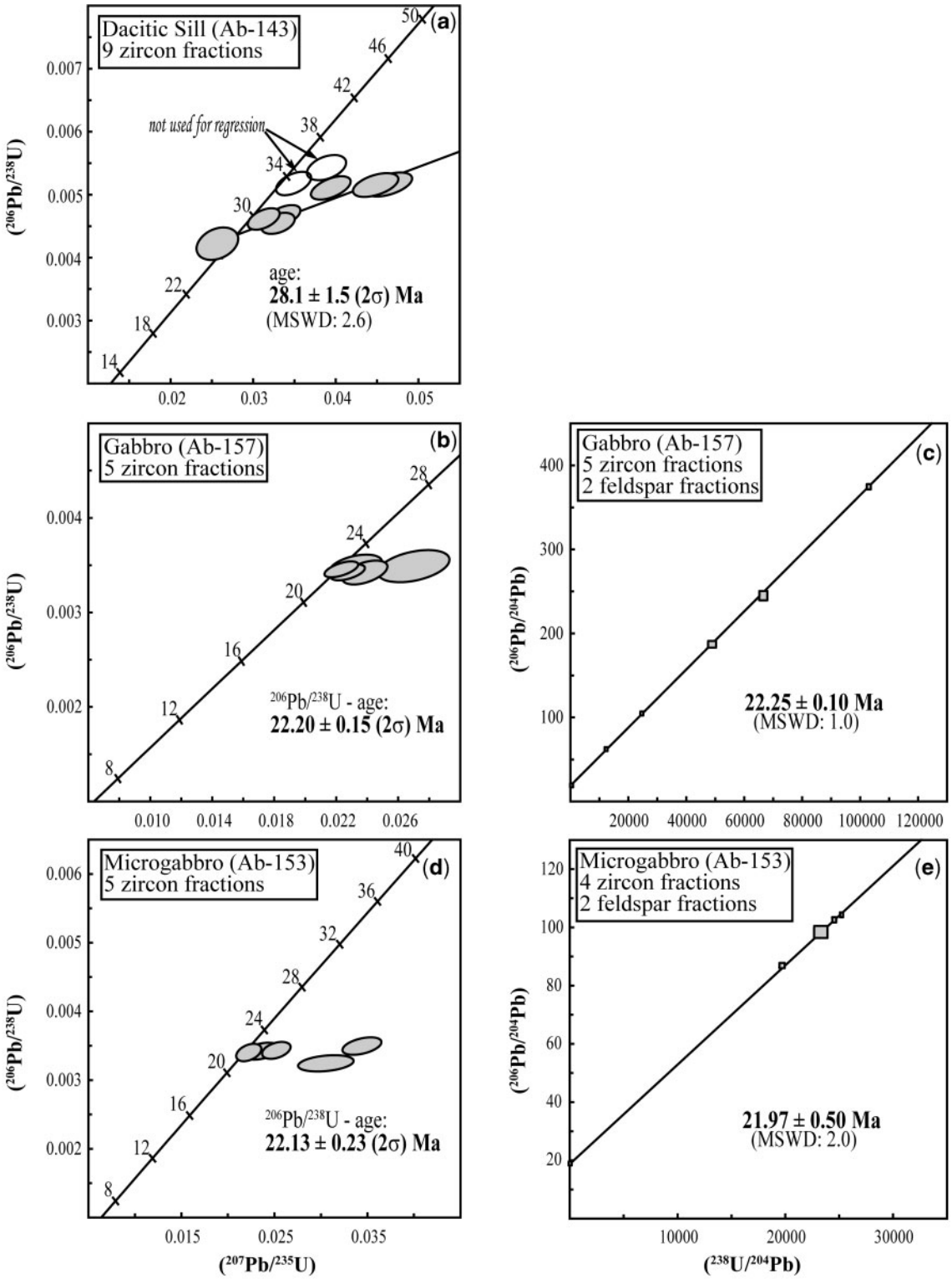

Fig. 3. Concordia and isochron diagrams for U–Pb dating of zircon and plagioclase (Tables 2 and 3). Ellipses (correlated errors) and error boxes (uncorrelated errors) correspond to 2σ-STERR of the mean ratios. Linear regression calculations were performed with ISOPLOT-3 (Ludwig, 2003).

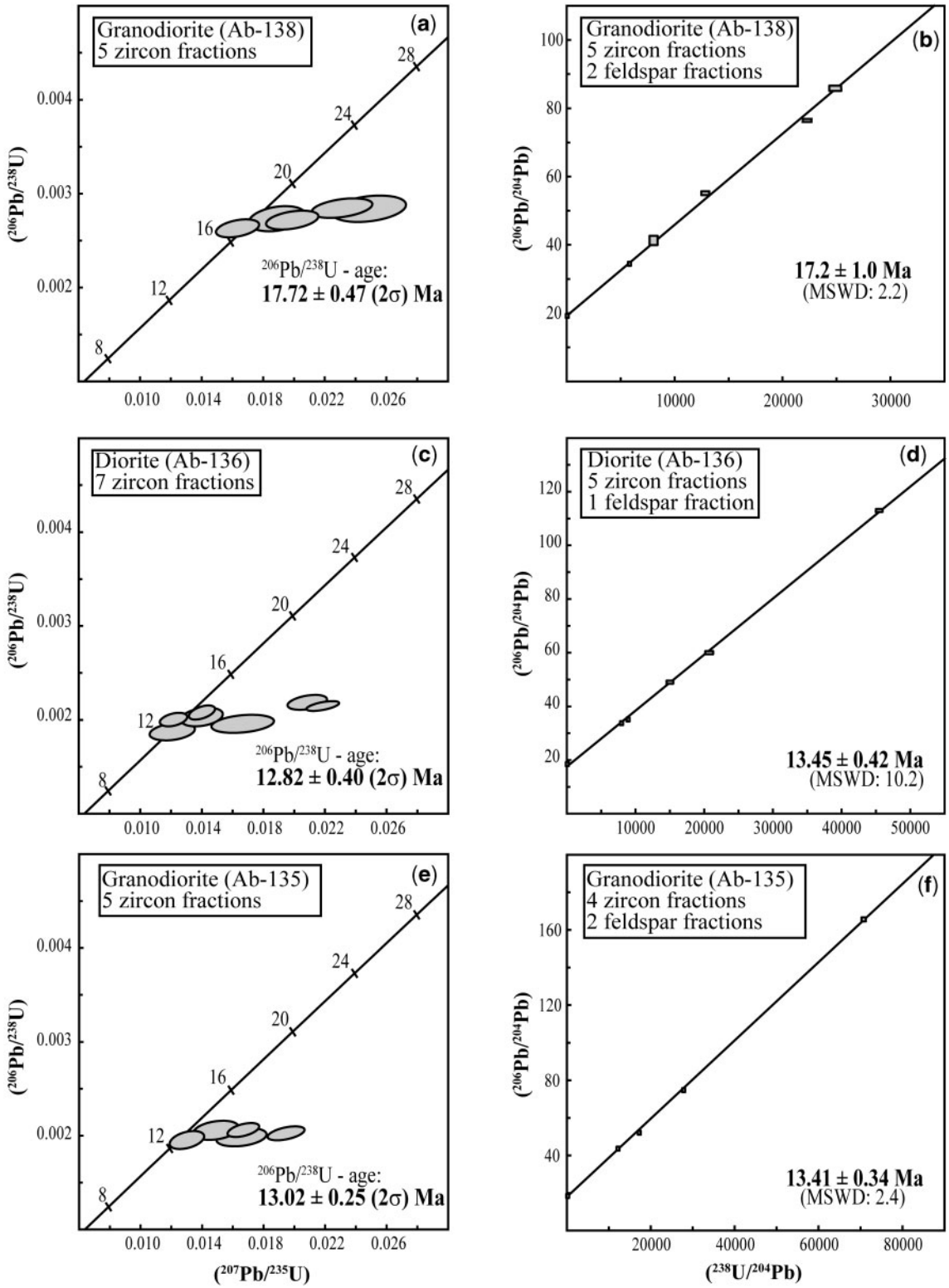

Fig. 4. Concordia and isochron diagrams for U–Pb dating of zircon and plagioclase (Tables 2 and 3). Ellipses (correlated errors) and error boxes (uncorrelated errors) correspond to 2σ-STERR of the mean ratios. Linear regression calculations were performed with ISOPLOT-3 (Ludwig, 2003).

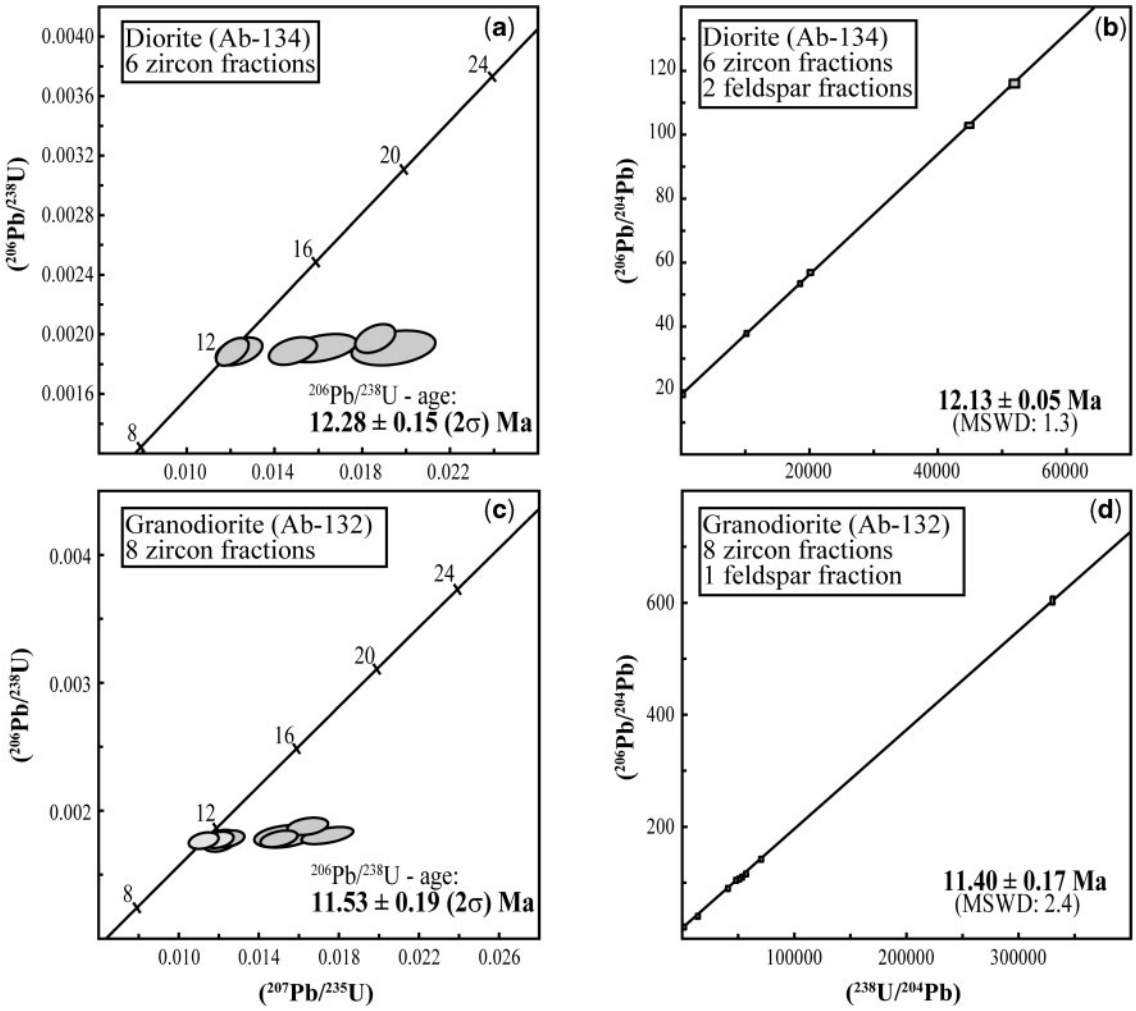

Fig. 5. Concordia and isochron diagrams for U–Pb dating of zircon and plagioclase (Tables 2 and 3). Ellipses (correlated errors) and error boxes (uncorrelated errors) correspond to 2σ-STERR of the mean ratios. Linear regression calculations were performed with ISOPLOT-3 (Ludwig, 2003).

(1–2 mm). Secondary calcite and sericite are observed in strongly altered plagioclase. Accessory minerals are apatite, zircon and titanite.

(5) Two samples, a micro-gabbro (Ab-153) and a gabbro (Ab-157), were collected from two fine- to medium-grained intrusions, respectively. Plagioclase is fresh in both rocks and shows a poikilitic texture with interstitial augite, whereas clinopyroxene has some minor secondary epidote.

(6) A tremolite-andesite hornfels sample (Ab-139) was collected from the metamorphic contact aureole around a granodioritic body intruding intermediate volcanic rocks; this has a fine-grained granoblastic texture. The most common contact metamorphic minerals are tremolite and biotite occurring together with primary andesine. The contact metamorphic rocks are fresh, showing some minor epidote, sericite, chlorite and pumpellyite in rare altered domains.

(7) Three samples (Ab-138, -132, -135) were taken from different homogeneous medium-grained granodioritic stocks that are much less altered than the volcanic members. Their constituent biotite and amphibole is replaced to varying degrees by chlorite, epidote and calcite. Plagioclase shows minor secondary smectite and calcite. Accessory phases are apatite, titanite, and zircon.

(8) Two fine- to medium-grained diorites (Ab-134, -136) were collected from the uppermost part of the series; these contain fresh plagioclase, clinopyroxene (augite) and orthopyroxene with epidote–chlorite alteration. Accessory phases are apatite and zircon.

Major and trace elements

Table 1 lists the major and trace element compositions of eight rocks taken from different levels of the volcanic sequence; Fig. 2 shows these data in a TAS diagram (a),

Table 1: Representative major and trace element data for whole-rock samples from the Abanico Formation

Sample:	Ab-45	Ab-47	Ab-49	Ab-53	Ab-56	Ab-77	Ab-86	Ab-110
Lithology:	Trachy-andesite	Basaltic trachy-andesite	Basaltic trachy-andesite	Andesite	Trachy-andesite	Basalt	Basalt	Basaltic andesite
wt%								
SiO_2	58·31	51·58	53·01	61·88	56·51	46·18	46·15	56·32
TiO_2	0·79	3·27	2·05	1·12	1·07	1·55	1·25	1·26
Al_2O_3	17·79	19·32	18·49	15·42	16·49	17·92	17·65	17·68
Fe_2O_3	6·65	5·39	5·88	3·93	6·79	9·68	8·19	3·43
FeO	1·20	2·52	3·36	2·92	4·08	1·20	1·20	4·68
MnO	0·15	0·30	0·27	0·26	0·18	0·12	0·13	0·21
MgO	2·34	3·47	2·92	1·87	2·79	4·41	7·41	2·28
CaO	3·42	3·93	3·97	3·71	1·62	11·5	10·0	6·38
Na_2O	4·36	4·46	4·73	4·45	6·49	3·48	3·36	4·10
K_2O	2·46	1·86	1·49	2·06	0·98	0·16	0·54	1·34
P_2O_5	0·35	0·33	0·30	0·48	0·41	0·28	0·19	0·33
LOI	1·90	3·34	3·32	1·65	2·23	3·08	3·49	1·76
Total	99·72	99·77	99·79	99·75	99·64	99·56	99·56	99·77
ppm								
Y	19·2	19·3	18·7	38·2	23·4	17·1	13·2	25·1
Sc	12·1	14·4	15·5	23·2	17·3	25·2	27·1	24·1
Nb	8·41	5·85	5·22	5·21	5·22	144	10·1	4·72
Th	2·51	2·22	1·71	2·42	4·14	2·22	2·05	2·12
Hf	4·9·1	2·85	2·44	5·12	3·64	3·11	2·44	2·91
Zn	71·1	81·2	74·4	158	50·1	96·1	79·2	123
Co	13·1	17·2	21·2	12·4	17·4	30·4	30·5	17·6
Ni	5·42	9·55	5·76	7·53	10·7	47·5	113	<2
Ba	603	481	362	416	236	130	370	300
Cr	9·44	3·45	7·23	7·45	7·25	90·1	290	6·23
V	106	154	157	33·5	158	240	221	87·2
Cu	5·25	3·78	<2	<2	<2	33·4	20·7	11·5
Sr	512	291	194	344	111	570	650	370
Zr	147	119	102	151	113	131	104	133
La	22·7	17·4	15·6	20·2	17·3	14·7	10·7	13·7
Ce	47·5	39·6	35·5	48·3	39·5	35·3	26·4	33·2
Nd	26·7	222	20·2	32·6	22·2	19·3	15·4	20·6
Sm	5·26	4·53	4·04	7·16	4·93	4·08	3·08	4·72
Eu	1·44	1·34	1·37	2·25	1·27	1·29	1·04	1·49
Gd	3·69	3·69	3·68	7·25	4·58	4·27	3·08	4·95
Dy	3·74	3·73	3·61	7·41	7·5	3·74	2·98	5·16
Ho	0·81	0·77	0·72	1·46	0·85	0·73	0·52	1·03
Er	2·33	2·23	1·99	4·11	2·31	1·57	1·18	2·42
Yb	2·25	2·13	1·89	4·01	2·27	1·51	1·18	2·45
Lu	0·35	0·31	0·29	0·62	0·36	0·22	0·16	0·34

an AFM diagram (b), and chondrite-normalized REE patterns (c). Basaltic to trachyandesitic rocks contain between 46 and 62 wt% SiO_2, and plot within the field defined by all previously analyzed rocks from the Abanico and Farellones Formations at 33–36°S. Their REE patterns are enriched in light REE (LREE) relative to HREE, and are characterized by $(La/Yb)_N$ ratios ranging between 3·6 and 7·0 (Fig. 2c). LREE enrichment abundance reaches about 90 times chondrite; the HREE in the basaltic rocks lie at about six times chondrite abundance,

whereas the more differentiated lithologies, such as trachyandesites, reach an enrichment factor of 24 for HREE (Fig. 2c) with a somewhat flatter pattern than the less differentiated rocks. A notable observation is the total absence of significant Eu anomalies in all samples.

U–Pb dating

Table 2 summarizes the zircon U–Pb analytical results used for the concordia plots, and Table 3 shows those samples for which $^{206}Pb/^{204}Pb$ (α)–$^{238}U/^{204}Pb$ (μ) isochrons were calculated, including initial Pb ratios measured in cogenetic feldspars (Table 4). These results were obtained on 50 size fractions of zircon. Figures 3–5 display the concordia and isochron diagrams. Size-fractions of the 0·05 and 0·20 mm long zircon crystals vary in weight between 0·042 and 0·949 mg, representing between 20 and 100 grains. Cracks were absent and all grains analyzed were euhedral prisms ranging in width to length ratio between 1:1 and 4:1. Most zircons were pinkish translucent grains, and only the dacitic sill (Ab-143) had transparent colorless grains. Opaque and translucent inclusions, excluded from analysis as far as possible, were present in all populations. Independent of grain size and lithology, both types of inclusion reach about 5 vol. %, with most opaque inclusions being of clinopyroxene, and translucent grains of apatite.

Nine zircon fractions from a dacitic sill (Ab-143) lying conformably within olivine-basalt lavas yield both concordant and differently discordant data. Scatter in $^{206}Pb/^{238}U$ prevents the use of the α–μ isochron plot. On the other hand, seven of the fractions define a regression line that intercepts the concordia curve at $28{\cdot}1 \pm 1{\cdot}5$ (2σ) Ma (MSWD = 2·6). Uranium concentrations lie between 320 and 704 ppm. Total common Pb is 28–370 pg and measured $^{206}Pb/^{204}Pb$ ratios range from 48·9 to 457.

A gabbroic intrusive body (Ab-157) occurring within basaltic flows of the lowermost Abanico Formation yields three identically concordant zircon fractions, and a slightly discordant age. All $^{206}Pb/^{238}U$ values are identical, whereas $^{207}Pb/^{235}U$ shows up to 5% scatter. The mean value of the five zircon $^{206}Pb/^{238}U$ ratios defines an age of $22{\cdot}20 \pm 0{\cdot}15$ Ma, and the corresponding α–μ isochron age, including feldspar, is $22{\cdot}25 \pm 0{\cdot}1$ (2σ) Ma (MSWD = 1·0), identical to the concordia age. Uranium concentration is between 307 and 683 ppm, total common Pb is 159–495 pg, and measured $^{206}Pb/^{204}Pb$ lies between 54·9 and 307.

Five zircon fractions from a micro-gabbro (Ab-153) emplaced into andesitic lava flows of the uppermost Abanico section produced two concordant and one slightly discordant dates, with the two remaining fractions showing scatter in $^{207}Pb/^{235}U$. One of these fractions also has a slightly younger $^{206}Pb/^{238}U$ age. In using the four zircons with identical $^{206}Pb/^{238}U$, an average age of $22{\cdot}13 \pm 0{\cdot}23$ Ma is obtained and an age of $21{\cdot}97 \pm 0{\cdot}50$ Ma (MSWD = 2·0) is given by the α–μ isochron plot. Uranium concentrations are between 335 and 361 ppm, total common Pb ranges from 166 to 251 pg, and measured $^{206}Pb/^{204}Pb$ lies between 42 and 92.

A granodiorite (Ab-138) cutting the uppermost andesitic lavas of the Abanico Formation yields two identically concordant zircon analyses, a slightly discordant date, and two analyses that show significant scatter in $^{207}Pb/^{235}U$. The five identical $^{206}Pb/^{238}U$ ratios yield an average age of $17{\cdot}72 \pm 0{\cdot}47$ Ma, and together with its cogenetic plagioclase they give an α–μ isochron age of $17{\cdot}2 \pm 1{\cdot}0$ Ma (MSWD = 2·2). Uranium ranges between 213–521 ppm, total common Pb 188–724 pg, and measured $^{206}Pb/^{204}Pb$ from 33·4 to 80·3.

From a diorite (Ab-136), emplaced into the uppermost layers of the Abanico Formation, four of seven zircon fractions plot concordantly, whereas the remaining three fractions exhibit up to 12% scatter in $^{207}Pb/^{235}U$. The average $^{206}Pb/^{238}U$ age of the five most concordant fractions is $12{\cdot}82 \pm 0{\cdot}40$ Ma, and together with plagioclase they give a α–μ isochron age of $13{\cdot}45 \pm 0{\cdot}42$ Ma (MSWD = 10·2). Uranium concentrations are 233–401 ppm, total common Pb is 66·0–404 pg, and measured $^{206}Pb/^{204}Pb$ lies between 31·7 and 171.

Five zircon fractions of a granodiorite (Ab-135) cutting andesitic flows in the upper Abanico Fm. yield a tight cluster of $^{206}Pb/^{238}U$ ratios but $^{207}Pb/^{235}U$ again shows scatter, reaching 7%. The average $^{206}Pb/^{238}U$ age of the five zircon fractions is $13{\cdot}02 \pm 0{\cdot}25$ Ma, identical to their zircon–plagioclase α–μ isochron age of $13{\cdot}41 \pm 0{\cdot}34$ Ma (MSWD = 2·4). Uranium concentrations are homogeneous at 223–282 ppm, total common Pb is 75·4–292 pg and measured $^{206}Pb/^{204}Pb$ lies between 40·2 and 106.

Sample Ab-134 is a diorite emplaced into basaltic flows of the lower Abanico series. All $^{206}Pb/^{238}U$ ratios are identical but $^{207}Pb/^{235}U$ shows large scatter of up to 20%. An age of $12{\cdot}28 \pm 0{\cdot}15$ Ma is defined by the mean value of the six $^{206}Pb/^{238}U$ ratios, and the α–μ isochron gives an age of $12{\cdot}13 \pm 0{\cdot}05$ (MSWD = 1·3). Uranium concentrations range from 259–318 ppm, total common Pb is 94·1–458 pg and measured $^{206}Pb/^{204}Pb$ ranges between 36·6 and 97·1.

Sample Ab-132 is a granodiorite intruding an olivine-basalt lava flow in the lower part of the Abanico Fm. Eight zircon fractions yield identical $^{206}Pb/^{238}U$ ages, but again $^{207}Pb/^{235}U$ shows scatter. The mean value of samples with identical $^{206}Pb/^{238}U$ ratios define an age of $11{\cdot}53 \pm 0{\cdot}19$ Ma, and the zircon–plagioclase α–μ isochron age is $11{\cdot}40 \pm 0{\cdot}17$ Ma (MSWD = 2·4). Uranium concentrations are 178–278 ppm, total common Pb is 25·2–302 pg, and measured $^{206}Pb/^{204}Pb$ lies between 37·0 and 233.

Pb, Sr, and Hf isotope data

Tables 4–6 list Pb, Sr, and Hf isotope data for 26 plagioclase separates and two clinopyroxene fractions for Pb,

Table 2: U–Pb analytical data for zircon mineral separates

Sample, zircon fraction*	Weight (mg)	Concentrations (ppm)			Measured	Radiogenic Pb (atomic%)§			Atomic ratios§		Apparent ages (Ma)	
		U	Pb rad	Pb_c (pg)†	($^{206}Pb/^{204}Pb$)‡	^{206}Pb	^{207}Pb	^{208}Pb	$^{206}Pb/^{238}U$	$^{207}Pb/^{235}U$	$^{206}Pb/^{238}U$	$^{207}Pb/^{235}U$
Dacitic sill (Ab-143)												
z-1, small size	0·042	556	2·75	28·4	260	81·1	4·3	14·7	0·004661	0·03374	30·0	33·7
z-2, small size	0·130	320	1·33	370	48·9	87·1	3·9	9·1	0·004217	0·02574	27·1	25·8
z-3, small size	0·244	498	2·71	136	310	81·3	4·0	14·7	0·005142	0·03479	33·1	34·7
z-4, small size	0·195	546	3·10	147	243	88·0	2·0	9·9	0·005157	0·04643	33·2	46·1
z-5, small size	0·158	379	2·12	99·1	215	79·2	5·0	15·8	0·005151	0·04487	33·1	44·6
z-6, small size	0·158	416	2·34	72·0	312	77·9	4·4	17·7	0·005102	0·03947	32·8	39·3
z-7, small size	0·175	704	3·51	82·0	457	79·6	3·9	16·5	0·004610	0·03136	29·6	31·4
z-8, small size	0·164	391	1·95	67·0	293	78·4	4·1	17·5	0·004540	0·03307	29·2	33·0
z-9, small size	0·185	413	2·42	156	186	79·3	4·1	16·6	0·005398	0·03876	34·7	38·6
Gabbro (Ab-157)												
z-1, medium size	0·364	642	2·57	253	218	73·5	3·5	23·0	0·003424	0·02277	22·0	22·9
z-2, medium size	0·178	307	1·26	329	54·9	72·8	4·9	22·3	0·003487	0·02704	22·4	27·1
z-3, medium size	0·296	611	2·48	495	99·1	73·9	3·6	22·5	0·003483	0·02328	22·4	23·4
z-4, medium size	0·346	606	2·48	159	307	72·7	3·4	23·9	0·003455	0·02236	22·2	22·5
z-5, medium size	0·321	683	2·73	311	171	73·8	3·7	22·5	0·003421	0·02387	22·0	24·0
Microgabbro (Ab-153)												
z-1, medium size	0·150	359	1·50	166	88·4	70·7	3·5	25·7	0·003420	0·02357	22·0	23·7
z-2, small size	0·060	337	1·43	173	42·5	65·7	4·5	29·8	0·003242	0·03057	20·9	30·6
z-3, small size	0·191	361	1·55	251	78·3	68·8	3·7	27·5	0·003432	0·02520	22·1	25·3
z-4, small size	0·202	340	1·43	202	91·5	69·6	3·3	27·1	0·003401	0·02223	21·9	22·3
z-5, small size	0·190	335	1·53	201	88·5	66·1	4·7	29·1	0·003493	0·03447	22·5	34·4
Granodiorite (Ab-138)												
z-1, small size	0·071	515	1·56	314	39·1	80·8	5·1	14·0	0·002838	0·02489	18·3	25·0
z-2, small size	0·111	296	0·91	188	49·5	79·8	4·7	15·5	0·002844	0·02315	18·3	23·2
z-3, small size	0·371	213	0·62	254	70·0	77·6	3·5	18·9	0·002631	0·01634	16·9	16·5
z-4, small size	0·243	521	1·62	352	80·3	75·1	4·0	20·9	0·002719	0·01989	17·5	20·0
z-5, small size	0·222	292	0·88	724	33·8	77·7	3·9	18·4	0·002731	0·01891	17·6	19·0
Diorite (Ab-136)												
z-1, medium size	0·949	303	0·69	305	58·7	75·7	3·3	20·9	0·002002	0·01213	12·9	12·2
z-2, medium size	0·193	312	0·76	283	45·8	72·2	3·6	24·2	0·002029	0·01399	13·1	14·1
z-3, medium size	0·245	304	0·79	66·0	171	71·1	5·3	23·6	0·002145	0·02188	13·8	22·0
z-4, medium size	0·131	401	0·85	404	34·0	76·4	3·6	20·1	0·001873	0·01206	12·1	12·2
z-5, medium size	0·090	233	0·54	197	31·7	73·1	4·5	22·4	0·001957	0·01665	12·6	16·8
z-6, medium size	0·247	307	0·76	135	92·0	72·2	3·5	24·3	0·002078	0·01400	13·4	14·1
z-7, medium size	0·296	296	0·80	113	125	69·8	4·8	25·4	0·002186	0·02086	14·1	21·0
Granodiorite (Ab-135)												
z-1, medium size	0·138	250	0·53	112	56·7	78·9	3·8	17·3	0·001958	0·01311	12·6	13·2
z-2, medium size	0·210	239	0·57	75·4	106	74·3	4·4	21·4	0·002064	0·01677	13·3	16·9
z-3, small size	0·179	228	0·51	245	40·2	78·8	4·2	17·1	0·002061	0·01500	13·3	15·1
z-4, small size	0·321	223	0·48	292	49·2	78·8	4·8	16·4	0·001989	0·01665	12·8	16·8
z-5, medium size	0·340	282	0·65	250	67·7	75·5	5·3	19·2	0·002030	0·01953	13·1	19·6

(continued)

Table 2: Continued

Sample, zircon fraction*	Weight (mg)	Concentrations (ppm)			Measured	Radiogenic Pb (atomic%)§			Atomic ratios§		Apparent ages (Ma)	
		U	Pb rad	Pb_c (pg)†	($^{206}Pb/^{204}Pb$)‡	^{206}Pb	^{207}Pb	^{208}Pb	$^{206}Pb/^{238}U$	$^{207}Pb/^{235}U$	$^{206}Pb/^{238}U$	$^{207}Pb/^{235}U$
Diorite (Ab-134)												
z-1, medium size	0·158	318	0·77	201	48·3	67·2	3·2	29·5	0·001883	0·01240	12·1	12·5
z-2, medium size	0·171	268	0·65	94·1	76·0	66·8	3·8	29·4	0·001887	0·01485	12·2	15·0
z-3, medium size	0·143	316	0·80	99·5	75·0	66·7	4·6	28·7	0·001971	0·01861	12·7	18·7
z-4, small size	0·265	259	0·65	458	36·6	65·6	4·8	29·6	0·001906	0·01943	12·3	19·5
z-5, small size	0·298	282	0·71	293	53·1	65·2	4·0	30·7	0·001905	0·01616	12·3	16·3
z-6, small size	0·350	292	0·69	155	97·1	68·4	3·2	28·4	0·001880	0·01212	12·1	12·2
Granodiorite (Ab-132)												
z-1, small size	0·282	178	0·34	87·1	82·0	79·4	3·9	16·7	0·001756	0·01190	11·3	12·0
z-2, small size	0·274	278	0·54	25·2	52·3	79·4	4·9	15·7	0·001777	0·01504	11·4	15·2
z-3, small size	0·229	248	0·52	84·3	99·0	77·3	4·9	17·8	0·001876	0·01647	12·1	16·6
z-4, small size	0·288	260	0·50	125	86·1	79·6	4·0	16·4	0·001780	0·01238	11·5	12·5
z-5, small size	0·225	214	0·38	302	37·0	86·0	5·3	8·7	0·001799	0·01530	11·6	15·4
z-6, small size	0·211	203	0·41	99·4	68·0	77·7	5·4	16·9	0·001805	0·01744	11·6	17·6
z-7, medium size	0·286	256	0·48	118	88·0	80·3	4·0	15·7	0·001760	0·01209	11·4	12·2
z-8, medium size	0·352	259	0·48	47·5	233	81·9	4·0	14·1	0·001770	0·01199	11·4	12·1

*Analyses were performed on crack-free, euhedral and mostly translucent zircons. Small size is 50–100 μm; medium size is 100–200 μm. Decay constants for ^{238}U and ^{235}U are those determined by Jaffey *et al*. (1971) as recommended by Steiger & Jäger (1977).
†Total amount of blank and intial Pb, corrected for mass discrimination and isotope tracer contribution.
‡Corrected for mass discrimination.
§Corrected for mass discrimination, isotopic tracer contribution, blank, and initial common lead such as determined in plagioclase of the dated rock. Further information on the analytical procedure is given in the text.

Table 3: U–Pb analytical data for isochron (α–μ) plots

Samples, zircon and plagioclase fractions*	U (ppm)	Pb_c (pg)†	$^{206}Pb/^{204}Pb$ (α)‡	Relative error in% (2σ)	$^{238}U/^{204}Pb$ (μ)‡	Relative error in% (2σ)
Gabbro (Ab-157)						
z-1, medium size	642	253	244·9	1·50	66063	1·2
z-2, medium size	307	329	61·50	0·29	12320	0·8
z-3, medium size	611	495	104·2	0·10	24564	1·8
z-4, medium size	606	159	374·3	0·51	102980	0·3
z-5, medium size	683	311	187·2	1·50	49295	1·4
plag.-1	–	–	18·675	0·18	–	–
plag.-2	–	–	18·575	0·03	–	–
Microgabbro (Ab-153)						
z-1, medium size	359	166	103·8	0·64	24964	0·42
z-3, small size	361	251	86·41	0·60	19744	0·50
z-4, small size	340	202	104·2	0·50	25195	0·30
z-5, small size	335	201	100·7	2·00	23530	1·30

(continued)

Table 3: Continued

Samples, zircon and plagioclase fractions*	U (ppm)	Pb_c (pg)†	$^{206}Pb/^{204}Pb$ (α)‡	Relative error in% (2σ)	$^{238}U/^{204}Pb$ (μ)‡	Relative error in% (2σ)
plag.-1	–	–	18·458	0·10	–	–
plag.-2	–	–	18·605	0·10	–	–
Granodiorite (Ab-138)						
z-1, small size	515	314	41·30	2·00	8033	3·00
z-2, small size	296	188	55·31	0·54	12970	1·50
z-3, small size	213	254	76·93	0·32	22237	0·80
z-4, small size	521	352	86·06	0·60	24838	1·00
z-5, small size	292	724	34·49	0·22	5852	0·30
plag.-1	–	–	18·439	0·10	–	–
plag.-2	–	–	18·427	0·10	–	–
Diorite (Ab-136)						
z-1, medium size	303	305	60·11	0·60	20765	1·20
z-2, medium size	312	283	49·02	0·91	15021	1·60
z-4, medium size	401	404	35·24	0·30	8910	0·60
z-5, medium size	233	197	34·04	0·20	7924	3·00
z-6, medium size	307	135	112·9	0·22	45444	0·20
plag.	–	–	18·538	0·13	–	–
Granodiorite (Ab-135)						
z-2, medium size	239	75·4	165·5	0·30	70677	0·30
z-3, small size	228	245	43·32	0·30	11977	0·60
z-4, small size	223	292	52·73	0·60	17159	0·40
z-5, medium size	282	250	74·48	0·91	27538	0·66
plag.-1	–	–	18·604	0·10	–	–
plag.-2	–	–	18·509	0·06	–	–
Gabbro (Ab-134)						
z-1, medium size	318	201	53·51	0·30	18572	0·30
z-2, medium size	268	94·1	102·8	0·45	44657	1·00
z-4, small size	259	458	37·90	0·46	10137	0·80
z-5, small size	282	293	57·02	0·50	20167	1·70
z-6, small size	292	155	116·0	0·86	51848	1·20
plag.-1	–	–	18·536	0·08	–	–
plag.-2	–	–	18·615	0·04	–	–
Granodiorite (Ab-132)						
z-1, small size	178	87·1	115·2	1·00	55060	1·10
z-3, small size	248	84·3	144·1	0·38	66895	0·43
z-4, small size	260	125	107·5	0·40	49985	2·10
z-5, small size	214	302	40·31	0·28	12070	0·31
z-6, small size	203	99·4	89·13	0·54	39072	0·45
z-7, medium size	256	118	111·4	0·77	52706	1·20
z-8, medium size	259	47·5	601·5	0·95	329595	0·46
plag.	–	–	18·538	0·01	–	–

*As described in Table 2.
†Total amount of blank and initial common Pb in picograms.
‡Corrected for mass discrimination, isotope tracer contribution, and blank.

Table 4: Pb isotope data for feldspar and clinopyroxene

Samples, mineral fractions*	Weight (mg)	Initial isotope ratios†			Source characteristics, single-stage model‡		
		$^{206}Pb/^{204}Pb$	$^{207}Pb/^{204}Pb$	$^{208}Pb/^{204}Pb$			
		α	β	γ	μ	ω	κ
Olivine basalt (Ab-99)							
clinopyroxene	8·2	18·644 ± 0·035	15·696 ± 0·036	38·606 ± 0·090	9·1	36·1	4·0
Gabbro sill (Ab-142)							
plag.-1	12	18·638 ± 0·020	15·626 ± 0·018	38·429 ± 0·046	9·1	35·4	3·9
Pyroxene andesite (Ab-154)							
plag.-1	7·3	18·599 ± 0·033	15·833 ± 0·028	38·793 ± 0·068	9·0	36·8	4·1
Pyroxene andesite (Ab-156)							
plag.-1	9·5	18·574 ± 0·019	15·626 ± 0·022	38·402 ± 0·029	9·0	35·3	3·9
plag.-2	10	18·566 ± 0·016	15·609 ± 0·015	38·484 ± 0·033	9·0	35·6	3·9
Pyroxene andesite (Ab-159)							
plag.-1	9·6	18·436 ± 0·018	15·582 ± 0·016	38·266 ± 0·047	8·9	34·7	3·9
plag.-2	9·1	18·448 ± 0·030	15·596 ± 0·016	38·356 ± 0·028	8·9	35·1	3·9
Dacitic sill (Ab-133)							
plag.-1	10	19·023 ± 0·029	15·609 ± 0·025	38·735 ± 0·063	9·5	36·6	3·9
plag.-2	12	18·918 ± 0·024	15·672 ± 0·011	38·793 ± 0·051	9·4	36·8	3·9
plag.-3	8·2	18·827 ± 0·013	15·653 ± 0·021	38·580 ± 0·038	9·3	36·0	3·9
Dacitic sill (Ab-143)							
plag.-1	19	18·942 ± 0·022	15·648 ± 0·016	39·036 ± 0·044	9·4	37·8	4·0
plag.-2	19	18·924 ± 0·022	15·645 ± 0·019	39·084 ± 0·046	9·4	38·0	4·1
Andesitic sill (Ab-152)							
plag.-1	9·6	18·601 ± 0·010	15·621 ± 0·010	38·508 ± 0·018	9·0	35·7	4·0
plag.-2	9·2	18·583 ± 0·033	15·640 ± 0·022	38·464 ± 0·058	9·0	35·5	3·9
Gabbro (Ab-157)							
plag.-1	9·4	18·675 ± 0·034	15·700 ± 0·029	38·644 ± 0·065	9·1	36·2	4·0
plag.-2	9·5	18·575 ± 0·010	15·611 ± 0·010	38·489 ± 0·011	9·0	35·6	4·0
Microgabbro (Ab-153)							
plag.-1	9·9	18·458 ± 0·018	15·593 ± 0·013	38·249 ± 0·041	8·9	34·7	3·9
plag.-2	9·5	18·605 ± 0·018	15·636 ± 0·014	38·456 ± 0·031	9·0	35·5	3·9
Andesitic hornfels (Ab-139)							
plag.-1	8·0	18·358 ± 0·012	15·569 ± 0·009	38·508 ± 0·027	8·8	35·7	4·0
Granodiorite (Ab-138)							
plag.-1	9·0	18·439 ± 0·018	15·582 ± 0·015	38·434 ± 0·037	8·9	35·4	4·0
plag.-2	8·8	18·427 ± 0·016	15·607 ± 0·015	38·279 ± 0·035	8·9	34·8	3·9
Diorite (Ab-136)							
plag.-1	10	18·538 ± 0·024	15·619 ± 0·024	38·342 ± 0·054	8·9	35·0	3·9
Granodiorite (Ab-135)							
plag.-2	11	18·604 ± 0·017	15·607 ± 0·017	38·428 ± 0·042	9·0	35·4	3·9
plag.-3	9·6	18·509 ± 0·011	15·567 ± 0·008	38·285 ± 0·016	9·0	34·8	3·9
Diorite (Ab-134)							
plag.-1	10	18·536 ± 0·014	15·592 ± 0·015	38·530 ± 0·034	9·0	35·8	4·0
plag.-2	9·8	18·615 ± 0·010	15·656 ± 0·010	38·599 ± 0·010	9·0	36·1	4·0
clinopyroxene	12	18·622 ± 0·042	15·682 ± 0·040	38·580 ± 0·032	9·0	36·0	4·0
Granodiorite (Ab-132)							
plag.-1	10	18·538 ± 0·010	15·639 ± 0·006	38·540 ± 0·017	9·0	35·8	4·0

*Selected fractions of fresh grains.
†Ratios corrected for mass discrimination and Pb blank, and where spiked, for isotope tracer contribution. Absolute error on α, β and γ ratios with 2σ significance.
‡All μ ($^{238}U/^{204}Pb$), ω ($^{232}Th/^{204}Pb$) and κ ($^{232}Th/^{238}U$) values were calculated using the single-stage evolution model of the Earth mantle (Holmes, 1946) and an age of 4·56 Ga. Primordial Pb isotopic compositions are taken from Tatsumoto *et al*. (1973).

Table 5: Sr analytical data for feldspar and clinopyroxene

Sample	Mineral	$(^{87}Sr/^{86}Sr)_{norm.} = (^{87}Sr/^{86}Sr)_{i\ (2\sigma\text{-STERR})}$
Olivine basalt (Ab-99)	clinopyroxene	0·70401 ± 3
Gabbro sill (Ab-142)	plagioclase	0·70369 ± 2
Pyroxene andesite (Ab-154)	plagioclase	0·70406 ± 2
Pyroxene andesite (Ab-156)	plagioclase	0·70414 ± 2
Pyroxene andesite (Ab-159)	plagioclase	0·70430 ± 1
Dacitic sill (Ab-133)	plagioclase	0·70662 ± 4
Dacitic sill (Ab-143)	plagioclase	0·70660 ± 2
Andesitic sill (Ab-152)	plagioclase	0·70505 ± 2
Gabbro (Ab-157)	plagioclase	0·70441 ± 3
Microgabbro (Ab-153)	plagioclase	0·70378 ± 3
Duplicate (Ab-15)3	plagioclase	0·70402 ± 4
Andesitic hornfels (Ab-139)	plagioclase	0·70459 ± 2
Granodiorite (Ab-138)	plagioclase	0·70420 ± 1
Diorite (Ab-136)	plagioclase	0·70466 ± 1
Granodiorite (Ab-135)	plagioclase	0·70427 ± 4
Duplicate(Ab-135)	plagioclase	0·70391 ± 2
Diorite (Ab-134)	plagioclase	0·70388 ± 5
Duplicate (Ab-134)	plagioclase	0·70421 ± 4
Diorite (Ab-134)	clinopyroxene	0·70429 ± 2
Granodiorite (Ab-132)	plagioclase	0·70405 ± 2

To correct for mass-fractionation, measured $^{87}Sr/^{86}Sr$ ratios were normalized to $^{86}Sr/^{88}Sr = 0{\cdot}1194$. Uncertainties for $(^{87}Sr/^{86}Sr)_{norm.}$ are given relative to the last digit.

18 plagioclase and two clinopyroxene fractions for Sr, and 20 zircon fractions for Hf. Duplicate analyses were performed for all isotope systems, using different size fractions of the same mineral population, to trace any potential heterogeneity in the initial isotope signatures on the rock scale; that is, minerals extracted from a few kilograms of rock. Figure 6 shows the εHf_i values plotted relative to the evolution of a chondritic uniform reservoir (CHUR), and the model for a continuously LILE-depleted mid-ocean ridge basalt (MORB) source mantle (DePaolo & Wasserburg, 1976; Patchett *et al.*, 1981). All εHf_i values are positive, ranging between +6·9 and +9·6. Figures 7–11 display correlation diagrams for Pb, Sr, and Hf isotope data, compared with previous data from the Oligo-Miocene magmatic belt (O-M belt), Pacific MORB source mantle, ocean island basalt (OIB) mantle sources, Pacific sediments, and reference values for subcontinental lithospheric mantle. This last field includes the initial isotope signatures of group I kimberlitic magmas (Smith, 1983; Weis & Demaiffe, 1985; Davies *et al.*, 2001; Schmidberger *et al.*, 2001), megacrystic clinopyroxene extracted from kimberlites (Kramers *et al.*, 1983; Davies *et al.*, 2001), magmatic perovskite (Heaman, 1989)

Table 6: Hf isotope analytical data for zircon

Sample	$(^{176}Hf/^{177}Hf)_{norm}$*	$^{206}Pb/^{238}U$ age (Ma)	$\varepsilon Hf_i \pm 2\sigma$ STERR†
Granodiorite (Ab-132)			
Z132-1	0·282967 ± 5	11·5	+7·1 ± 0·2
Z132-2	0·282959 ± 2	11·5	+6·9 ± 0·1
Diorite (Ab-134)			
Z134-1	0·282986 ± 5	12·3	+7·8 ± 0·2
Z134-2	0·282993 ± 4	12·3	+8·1 ± 0·1
Diorite (Ab-136)			
Z136-1	0·282999 ± 5	12·8	+8·3 ± 0·2
Granodiorite (Ab-135)			
Z135-1	0·282991 ± 4	13·0	+8·0 ± 0·1
Z135-2	0·282980 ± 4	13·0	+7·7 ± 0·1
Granodiorite (Ab-138)			
Z138-1	0·283007 ± 4	17·7	+8·7 ± 0·1
Z138-2	0·283032 ± 5	17·7	+9·6 ± 0·2
Microgabbro (Ab-153)			
Z153-1	0·282999 ± 6	22·1	+8·5 ± 0·2
Z153-2	0·282971 ± 9	22·1	+7·6 ± 0·3
Gabbro (Ab-157)			
Z157-1	0·283030 ± 5	22·2	+9·6 ± 0·2
Z157-2	0·283027 ± 3	22·2	+9·5 ± 0·1
Dacitic sill (Ab-143)			
Z143-1	0·282969 ± 5	28·1	+7·7 ± 0·2
Z143-2	0·282976 ± 4	28·1	+8·0 ± 0·2
Pyroxene andesite (Ab-156)			
Z156-1	0·283021 ± 5	n.d.	+9·5 ± 0·2
Pyroxene andesite (Ab-159)			
Z159-1	0·282955 ± 7	n.d.	+7·1 ± 0·2
Dacitic sill (Ab-133)			
Z133-1	0·282961 ± 3	n.d.	+7·4 ± 0·1
Z133-2	0·282955 ± 3	n.d	+7·2 ± 0·1
Andesitic sill (Ab-152)			
Z152-1	0·282946 ± 3	n.d.	+6·9 ± 0·1

*Measured $^{176}Hf/^{177}Hf$ corrected for mass discrimination using $^{179}Hf/^{177}Hf = 0{\cdot}7325$ (Patchett & Tatsumoto, 1980). JMC-475 Hf standard: $^{176}Hf/^{177}Hf = 0{\cdot}282162 \pm 1$ ($n = 9$). Uncertainties for $(^{176}Hf/^{177}Hf)_{norm.}$ are given relative to the last digit.

†To calculate εHf_i from $(^{176}Hf/^{177}Hf)_{norm}$ the following constants were used: age of the Earth = 4·56 Ga, present-day $(^{176}Lu/^{177}Hf)_{CHUR} = 0{\cdot}0332 \pm 2$; present-day $(^{176}Hf/^{177}Hf)_{CHUR} = 0{\cdot}282772 \pm 29$, $(^{176}Hf/^{177}Hf)_{CHUR}$ at 4·56 Ga = 0·279718 ± 29 (Blichert-Toft & Albarède, 1997); $(\varepsilon Hf_i)^T_{sample} = [((^{176}Hf/^{177}Hf)^T_{sample}/(^{176}Hf/^{177}Hf)^T_{CHUR}) - 1] \times 10^4$, with $(^{176}Hf/^{177}Hf)^T_{CHUR} = (^{176}Hf/^{177}Hf)^0_{CHUR} - [(^{176}Lu/^{177}Hf)^0_{CHUR} \times (e^{\lambda T} - 1)]$ (Patchett *et al.*, 1981); $\lambda_{Lu} = 1{\cdot}93 \times 10^{-11}\ a^{-1}$ (Sguigna *et al.*, 1982), with T being the U–Pb age of the zircon.

n.d., not determined.

and clinopyroxene from peridotite xenoliths in the volcanic rocks of northern Chile (Lucassen *et al.*, 2005).

For samples lacking Hf isotope analyses, Nd isotope signatures were translated to εHf_i using the relationship $\varepsilon Hf_i \approx 2\varepsilon Nd_i$ for MORB sources, and $\varepsilon Hf_i = 1{\cdot}33\varepsilon Nd_i + 3{\cdot}19$ for OIB mantle sources (Patchett, 1983; Vervoort *et al.*, 1996, 1999). Differences in εHf_i between the two conversion models are relatively small (typically of the order of ≈ 1 εHf_i unit) but they exceed our analytical errors, which are of the order of 0·1–0·3 ε units (Table 6). Figure 7b also shows the initial isotopic compositions of lower crustal mafic granulite xenoliths brought to the surface by Miocene volcanic rocks of the pre-Cordillera in Argentina (32°S; Kay *et al.*, 1996). The field of initial isotopic compositions of MORB reflects present-day ratios of their mantle sources. Shifts in isotope signatures, extrapolated back to Oligocene times, are negligible, given the low U/Pb, Rb/Sr, and Lu/Hf of MORB source mantle. The same would apply if melting of early Cenozoic oceanic lithosphere was considered, for which residence times are too short to produce significantly different isotope signatures compared with the MORB sources from which they were extracted.

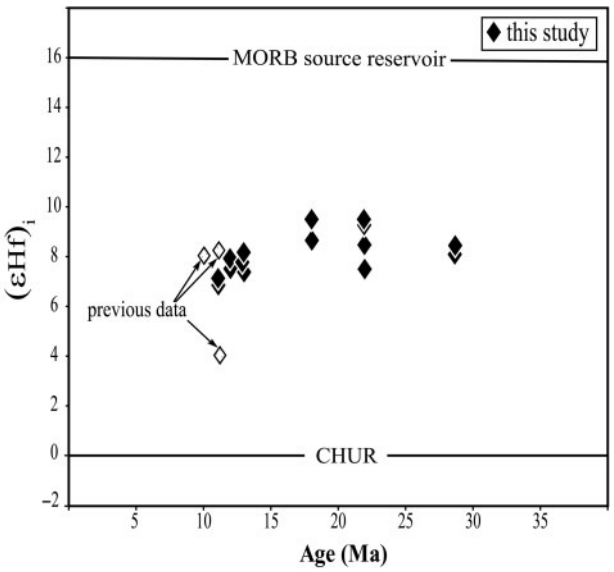

Fig. 6. Initial Hf isotope ratios as a function of zircon ages, expressed in εHf_i values relative to chondritic (CHUR), and MORB-source mantle reservoirs (Table 6). Open diamonds are previously published zircon data from the Oligo-Miocene magmatic belt of central Chile (Deckart & Godoy, 2006).

DISCUSSION

U–Pb dating

The following issues have to be considered concerning the U–Pb dating of the Oligo-Miocene zircons: (1) they contain very low amounts of radiogenic Pb produced since crystallization of the mineral; (2) relative to such low abundances of radiogenic Pb, initial common Pb is high; (3) ion beams must be sufficiently strong to be measured with sufficient accuracy, in particular for ^{204}Pb; (4) long dissolution times at high temperatures induce high Pb blanks. As a consequence of the low abundance of radiogenic Pb, the minimum weights of zircon fractions used were between 0·04 and 0·95 mg, requiring the use of relatively large amounts of ion-exchange resin adding a second Pb blank component. Although the Pb isotopic compositions of cogenetic feldspars were measured to allow common Pb corrections (Table 4), additional uncertainties are twofold: the Pb isotopic compositions of feldspar fractions of the same population can be different (Table 4), and inherited old Pb may be associated with different common initial Pb. Uncertainty in the common Pb correction is therefore the dominant analytical uncertainty for U–Pb dating using the concordia diagram. On the other hand, the determination of alternative isochron ages does not require this correction.

As revealed by the concordia plots, the scatter of $^{207}Pb/^{235}U$ in zircons from a given sample exceeds the expected uncertainties, such as those integrated into the error propagation (size of ellipses). This means that the $^{207}Pb/^{204}Pb$ ratios of initial common Pb cannot be determined with sufficient precision. From a purely analytical point of view, scatter of $^{207}Pb/^{235}Pb$ could also be due to interferences on the ^{207}Pb peak or bad peak shapes; however, both these parameters have been systematically controlled, as well as the quality of the mass base line. Because the $^{238}U-^{206}Pb$ chronometer is much less sensitive to common Pb corrections, no corresponding scatter is observed, and as a consequence all U–Pb ages are derived from the $^{206}Pb/^{238}U$ ratios. Alternative use of different common Pb isotopic compositions measured for feldspar fractions of the same rock does not change the concordia or isochron ages beyond the given analytical precisions. The new U–Pb ages range from 28·1 to 11·5 Ma, covering an Oligo-Miocene period of 16·6 Myr.

The 20 Hf isotope analyses (εHf_i) performed on the eight dated zircon populations, as well as on a further five zircons, yield εHf_i ranging between +6·9 and +9·6 (Fig. 6). A slight difference in εHf_i is observed even among zircon fractions separated from the same population (Ab-138; Ab-153, Table 6). Two of the previously published εHf_i values for 11–10 Ma granodiorite zircons from the same area are identical to those of this study, whereas one analysis has a less radiogenic value at +4·0 (Fig. 6; Deckart & Godoy, 2006).

Initial Pb isotope ratios (Pb_i) of plagioclase and clinopyroxene show a large range with all values being significantly more radiogenic than Pacific MORB. They are also distinct from Pacific OIB sources (Fig. 7). In the $^{206}Pb/^{204}Pb$ (α) vs $^{207}Pb/^{204}Pb$ (β) diagram (Fig. 7a), most Pb_i values lie in the range of model values for average and upper continental crust, with some Pb_i plotting

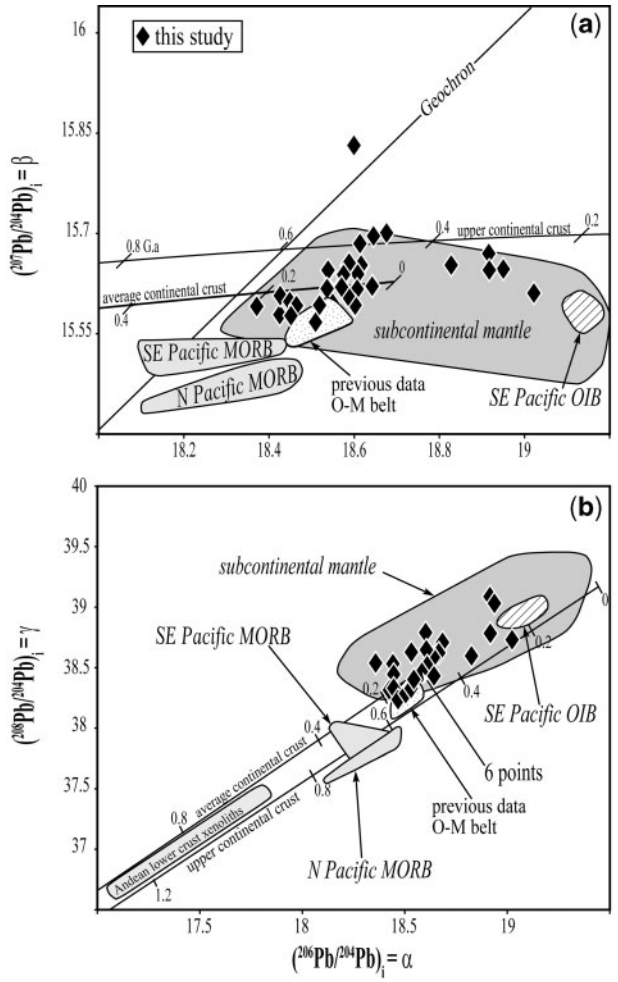

Fig. 7. (a, b) Initial Pb isotope ratios (α, β, γ) of plagioclase and clinopyroxene (Table 4) plotted relative to: (1) the geochron calculated for an Earth with age 4·56 Ga and primordial isotope ratios measured in the Canyon Diablo Fe-meteorite (Tatsumoto *et al.*, 1973), (2) model evolution curves for upper and average continental crust (Stacey & Kramers, 1975; Zartman & Doe, 1981), (3) Pacific MORB sources (Bach *et al.*, 1996; Karsten *et al.*, 1996; Chauvel & Blichert-Toft, 2001), (4) SE Pacific OIB sources (Gerlach *et al.*, 1986; Devey *et al.*, 2000), (5) reference values for subcontinental lithospheric mantle (Kramers *et al.*, 1983; Smith, 1983; Weis & Demaiffe, 1985; Heaman, 1989; Davies *et al.*, 2001; Schmidberger *et al.*, 2001; Lucassen *et al.*, 2005), and (6) previous data for the Oligo-Miocene magmatic belt (O-M belt) in central Chile (Vergara *et al.*, 1999; Nyström *et al.*, 2003; Kay *et al.*, 2005; Muñoz *et al.*, 2006). In (b) a field is included for present-day Pb isotopic compositions of Andean lower crustal xenoliths (Kay *et al.*, 1996).

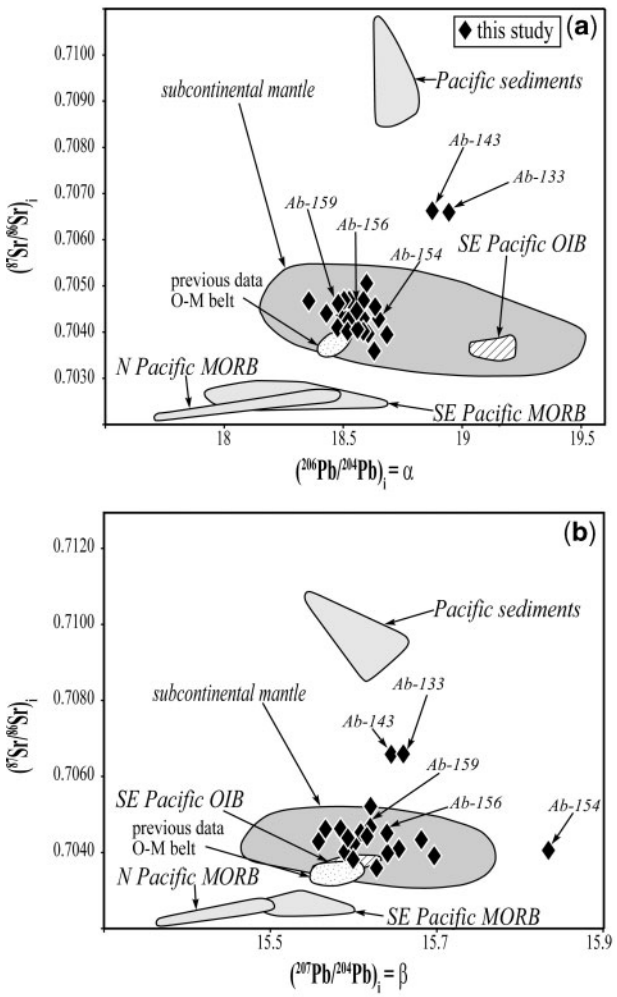

Fig. 8. (a, b) Correlation diagrams of initial Pb (α, β) vs initial $^{87}Sr/^{86}Sr$ isotope ratios of plagioclase and clinopyroxene (Tables 4 and 5), plotted relative to different potential magma sources including (1) Pacific MORB sources (Bach *et al.*, 1996; Karsten *et al.*, 1996; Chauvel & Blichert-Toft, 2001), (2) SE Pacific OIB sources (Gerlach *et al.*, 1986; Devey *et al.*, 2000), (3) Pacific sediments (Ben Othman *et al.*, 1989), (4) reference values for subcontinental lithospheric mantle (Kramers *et al.*, 1983; Smith, 1983; Weis & Demaiffe, 1985; Heaman, 1989; Davies *et al.*, 2001; Schmidberger *et al.*, 2001; Lucassen *et al.*, 2005), and (5) previous data for the Oligo-Miocene magmatic belt (O-M belt) in central Chile (Vergara *et al.*, 1999; Nyström *et al.*, 2003; Kay *et al.*, 2005; Muñoz *et al.*, 2006).

below average crust. In the α vs $^{208}Pb/^{204}Pb$ (γ) diagram (Fig. 7b) they lie at the upper end of the average crust model but they are distinct from the initial Pb isotopic compositions of Andean lower crustal xenoliths (Kay *et al.*, 1996). Previous Pb isotope data obtained for whole-rocks of the 28·8–5·2 Ma Oligo-Miocene magmatic sequence are identical to the least radiogenic values measured here, and again are distinct from both Pacific MORB and OIB sources. One exception is sample Ab-154, which has high ^{207}Pb (Fig. 7a). In the Pb_i vs Sr_i correlation diagram of Fig. 8 all initial isotope signatures are again distinct from any Pacific MORB source, and α is also different from Pacific OIB sources, whereas β lies very close to OIB. Large differences also exist relative to Pacific sediments. On the other hand, as already noted for Fig. 7, the data plot in the field of reference values for subcontinental lithospheric mantle.

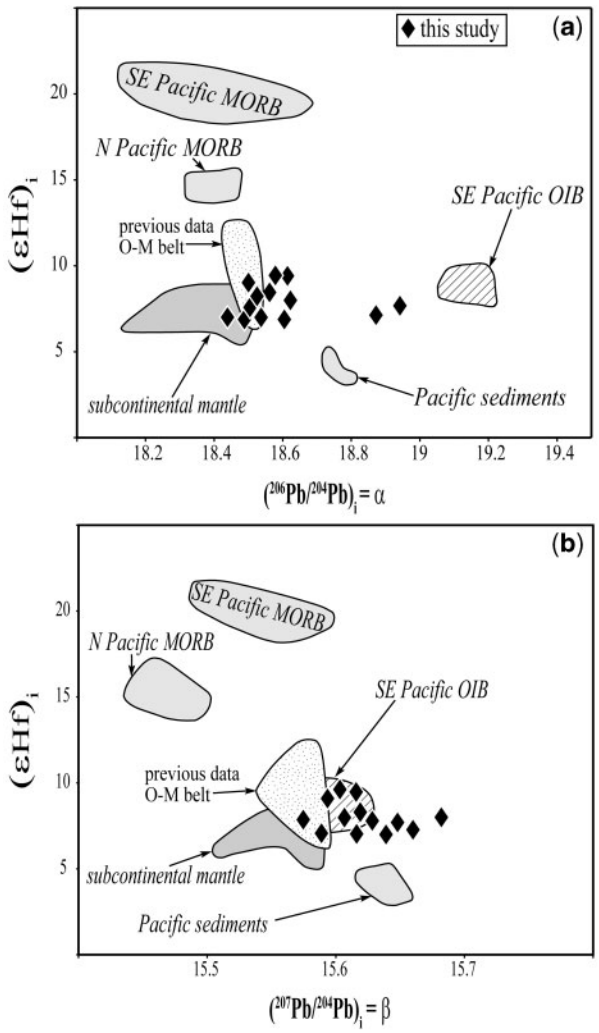

Fig. 9. (a, b) Correlation diagrams of initial Pb isotope ratios (α, β) vs εHf_i (initial $^{176}Hf/^{177}Hf$) of plagioclase and clinopyroxene for Pb, and zircon for Hf (Tables 4 and 6), plotted relative to different potential magma sources. To convert initial Nd isotope signatures of rocks for which no Hf data are available, we used the relationships $\varepsilon Hf_i \approx 2\varepsilon Nd_i$ for MORB sources and $\varepsilon Hf_i = 1{\cdot}33\varepsilon Nd_i + 3{\cdot}19$ for OIB mantle sources (Patchett, 1983; Vervoort *et al.*, 1996, 1999). Labelled fields are SE Pacific MORB (Bach *et al.*, 1996; Karsten *et al.*, 1996), SE Pacific OIB (Gerlach *et al.*, 1986; Devey *et al.*, 2000), and previous data for the Oligo-Miocene magmatic belt (Vergara *et al.*, 1999; Nyström *et al.*, 2003; Kay *et al.*, 2005; Muñoz *et al.*, 2006). Hf data are available for Pacific MORB (Chauvel & Blichert-Toft, 2001), Pacific sediments (White *et al.*, 1986), and xenocrystic zircons and baddeleyites from the Mbuji Mayi group-I kimberlite (Schärer *et al.*, 1997). Pb data for these subcontinental reservoirs are from Weis & Demaiffe (1985), Ben Othman *et al.* (1989) and Chauvel & Blichert-Toft (2001).

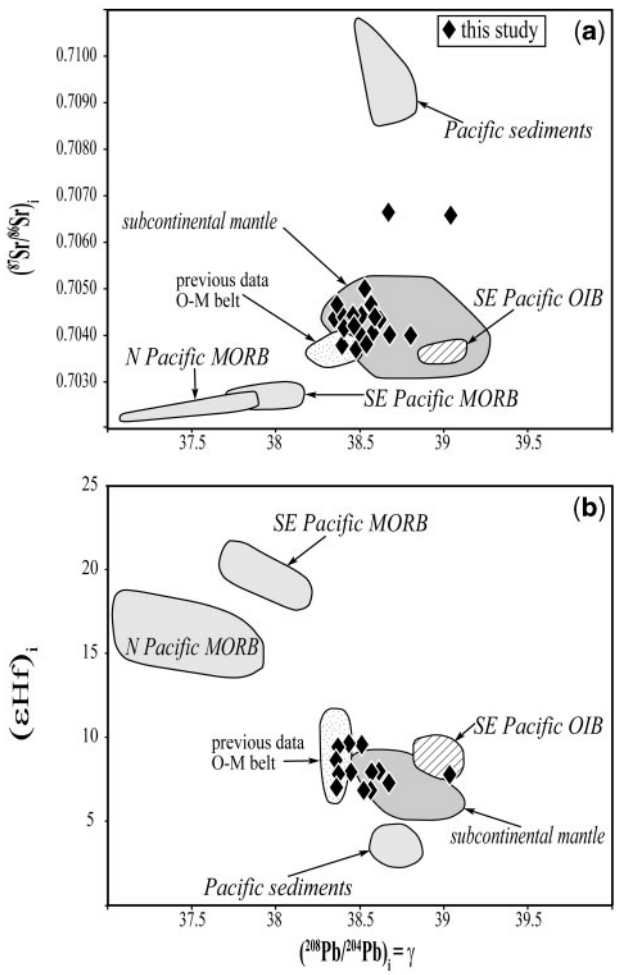

Fig. 10. Correlation diagrams for (a) initial Pb_i (γ) vs initial $^{87}Sr/^{86}Sr$, and (b) initial Pb_i (γ) vs εHf_i of plagioclase and clinopyroxene for Pb and zircon for Hf. Initial isotope signatures of the different potential magma sources shown are taken from the references cited in the captions of Figs 7–9.

Figure 9 displays Pb_i vs εHf_i data substantiating the same isotope differences already observed for α, β and γ as well as Pb_i–Sr_i correlations (Figs 7 and 8). For subsequent discussion it is important to note that for the initial Hf isotope ratios of subcontinental mantle only measured Hf isotope data were used. Lu/Sm fractionation in the subcontinental mantle is not sufficiently constrained to translate Nd isotope ratios into εHf_i (Nowell *et al.*, 2004). A particular observation is that in the α–εHf_i diagram, our Oligo-Miocene samples lie in, or very close to, the field of initial isotope signatures of zircon and baddeleyite megacrysts from the Central African Mbuji Mayi kimberlite (Weis & Demaiffe, 1985; Schärer *et al.*, 1997). In the β–εHf_i diagram the O-M belt zircons overlap with data from SE Pacific OIB sources, whereas they are distinct from any Pacific MORB source. In the γ–εHf_i and Sr_i–εHf correlation diagrams significant differences exist relative to both MORB or OIB mantle sources (Figs 10 and 11).

U–Pb ages

As already emphasized, the new U–Pb zircon dating was undertaken to determine unambiguous emplacement

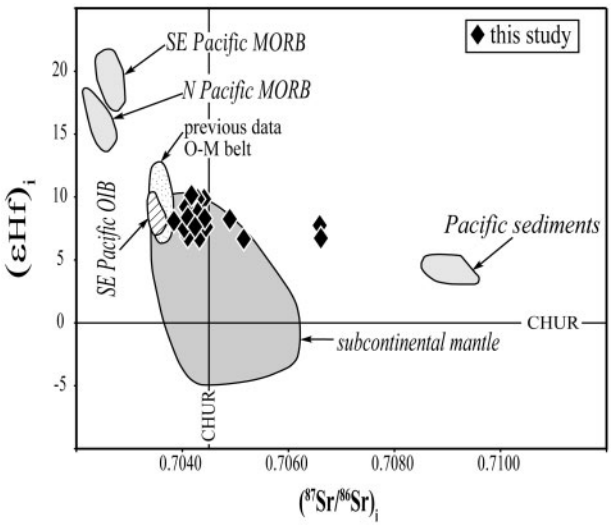

Fig. 11. Correlation diagram for initial $^{87}Sr/^{86}Sr$ vs εHf_i in plagioclase (Sr), clinopyroxene (Sr), and zircon (Hf). Initial isotope signatures of the different potential magma sources shown are taken from the references cited in the captions of Figs 7–9. Sr and Hf data defining the subcontinental lithospheric mantle field are from Weis & Demaiffe (1985), Schärer *et al.* (1997) and Nowell *et al.* (2004).

ages for the Oligo-Miocene magmatic rocks. Thus far, only U–Pb zircon ages could be considered to date the age of primary crystallization (Deckart *et al.*, 2005; Deckart & Godoy, 2006); whereas the interpretation of most previous K–Ar and $^{40}Ar/^{39}Ar$ whole-rock and mineral dates from central Chile remains uncertain because of the omnipresence of later low-grade metamorphism and hydrothermal activity (Drake *et al.*, 1976; Vergara & Drake, 1979; Munizaga & Vicente, 1982; Beccar *et al.*, 1986; Vergara *et al.*, 1988; Kurtz *et al.*, 1997; Fuentes *et al.*, 2002; Deckart *et al.*, 2005; Kay *et al.*, 2005; Muñoz *et al.*, 2006). For some older ages around 34 Ma, argon degassing patterns reveal the presence of significant excess ^{40}Ar, which rules out the determination of any geologically meaningful age ('maximum ages'; Gana & Wall, 1997; Muñoz *et al.*, 2006). In some cases, no age interpretation could be proposed; for example, for $^{40}Ar/^{39}Ar$ dating results of secondary minerals (Deckart *et al.*, 2005).

The new and all previous radiometric ages of the Oligo-Miocene magmatic rocks are summarized in Table 7 together with initial Sr, Pb, Nd, and Hf isotopic ratios, and model Th/U of the magma sources. Table 7 also distinguishes plutonic and volcanic lithologies. Previous zircon U–Pb ages (17–5 Ma; Deckart *et al.*, 2005) were also exclusively based on the $^{238}U–^{206}Pb$ chronometer, with the difference that no feldspars could be measured for Pb_i because of the strong metamorphic overprint of the rocks. The full set of radiometric ages substantiates basaltic–gabbroic to rhyolitic–granitic magmatic activity between 28·8 and 5·2 Ma, covering a period of 24 Myr during Oligo-Miocene times.

Abanico vs Farellones Formation

Based on field geology, radiometric ages, and isotope ratios it appears that both the volcanic and plutonic lithologies represent a continuous period of calc-alkaline magmatism, emplaced during Nazca–Farallon plate subduction beneath the South American continental margin. The distinction between the Abanico and Farellones Formations was originally based on differences in lithologies, observed between the lower and upper part of the volcanic–plutonic series (Hoffstetter *et al.*, 1957). The Farellones Formation was redefined by Rivano *et al.* (1990) with a distinction into a lower rhyolitic–dacitic to ignimbritic part, and an upper section composed of basaltic andesites, intruded by rhyodacitic domes. It was concluded that Abanico magmatism lasted from Oligocene times until 20 Ma, followed by emplacement of the Farellones Formation (Munizaga & Vicente, 1982; Vergara *et al.*, 1988; Fuentes *et al.*, 2002; Deckart *et al.*, 2005; Kay *et al.*, 2005). On the other hand, an overlap in emplacement ages was proposed for the same series about 100 km to the south of our study area, indicating that the lower Farellones and upper Abanico Formations have a similar age (Charrier *et al.*, 2002). A local angular unconformity at the base of the Farellones Formation was suggested (e.g. Aguirre, 1960), but other workers have questioned the existence of such an unconformity and proposed either a thrust at the base of the Farellones Formation or a stratigraphic contact (e.g. Godoy *et al.*, 1999). Our own detailed observations along the transition from the Abanico to the Farellones Formation do not reveal any unconformity or tectonic contact, and the zone seems to be a simple transition from older to younger magmatic series showing the same lithological spectrum. Given the uncertainties concerning both the distinction and age of the Abanico vs Farellones Formations, we consider that the dated rocks represent a continuum of magmatic activity.

Magma sources

The question arises whether lithological differences or isotope signatures are correlated in space and time. From our age data we cannot identify any clear compositional progression with time. The oldest (28·1 Ma) and youngest rocks (11·5 Ma) are both differentiated (i.e. a dacite and a granodiorite, respectively) and gabbros and diorites cover almost the full period of magmatism (22·2–12·3 Ma). An absence of correlation is also observed for isotope signatures and ages; however, previous geochemical data from the same magmatic belt suggested a continuous evolution from primitive rocks with $(La/Yb)_N = 3$, $(^{87}Sr/^{86}Sr)_i = 0{\cdot}7033$, and $\varepsilon Nd_i = +6{\cdot}2$ to slightly more evolved members having $(La/Yb)_N = 16$, $(^{87}Sr/^{86}Sr)_i = 0{\cdot}7044$, and $\varepsilon Nd_i = +3{\cdot}0$ (Nyström *et al.*, 2003; Kay *et al.*, 2005). Limited differences are also suggested

Table 7: Summary of ages and initial isotope characteristics of the Oligo-Miocene magmatic rocks of central Chile between 33° and 36° S

Dating method	Ages (Ma)		
	Previous ages of basalts to rhyolites	Previous ages of diorites to granites	This study; gabbros to granites + 1 dacite
K–Ar (whole-rock)	27·7–4·1	19·5–7·0	—
$^{40}Ar/^{39}Ar$ (minerals)	28·8–17·9 (plagioclase)	21·6–5·5 (hornblende, biotite)	—
U–Pb (zircon)	17·2–16·8	12·0–5·2	28·1–11·5
Isotope system	**Source signatures**		
	Previous whole-rock data for basalts to rhyolites	Previous whole-rock and zircon data for diorites to granites	This study; data for zircon, plagioclase and clinopyroxene
εNd_i	+3·0 to +6·2	+3·0 to +4·6	—
εHf_i	—	+4·0 to +8·0 (zircon)	+6·9 to +9·6
$(^{87}Sr/^{86}Sr)_i$	0·7033–0·7043	0·7039–0·7042	0·70369–0·70662
$(^{206}Pb/^{204}Pb)_i$ (α)	18·453–18·565	18·453–18·588	18·358–19·023
$(^{207}Pb/^{204}Pb)_i$ (β)	15·548–15·610	15·554–15·587	15·567–15·700
$(^{208}Pb/^{204}Pb)_i$ (γ)	38·262–38·478	38·210–38·388	38·249–39·084
$^{238}U/^{204}Pb$ (μ)	8·89–9·02	8·89–9·01	8·8–9·5
Th/U	3·88–3·94	3·86–3·89	3·9–4·1

Previous ages from Drake *et al*. (1976), Vergara & Drake (1979), Munizaga & Vicente (1982), Beccar *et al*. (1986), Vergara *et al*. (1988) and Kay *et al*. (2005) for K–Ar; from Gana & Wall (1997), Kurtz *et al*. (1997), Aguirre *et al*. (2000), Fuentes *et al*. (2002) and Muñoz *et al*. (2006) for $^{40}Ar/^{39}Ar$; from Deckart *et al*. (2005) for U–Pb. Initial isotope ratios for whole-rocks are from Vergara *et al*. (1999), Nyström *et al*. (2003), Kay *et al*. (2005) and Muñoz *et al*. (2006). Previous initial Hf isotope ratios in zircon from Deckart & Godoy (2006).

by the Pb isotopes signatures, with the older members being more homogeneous than the younger volcanic and plutonic lithologies (Nyström *et al*., 2003). This is consistent with the differences in lithology between the lower and upper parts of the succession (i.e. 80% basalt and 20% andesites in the lower part, and 20% basalt, 75% andesite, and 5% dacite in the upper part). All the isotopic data lie within the reference field for subcontinental lithospheric mantle.

Heterogeneities on the data from this study are also observed, with two dacites having more radiogenic Sr_i than the main cluster of data, and a pyroxene-andesite being more radiogenic in ^{207}Pb (Figs 7–11). For Sr in the dacites this deviation could be due either to a lithospheric mantle source that has evolved to a higher Rb/Sr but low U/Pb, or to the incorporation of a highly radiogenic crustal component. This latter hypothesis is in contradiction with the low radiogenic Pb_i measured in the same feldspar. Concerning the high ^{207}Pb, we necessarily need an old Precambrian source component, either in the metasomatized subcontinental mantle or as strongly Rb-depleted crustal material (lower crust?), to explain the absence of more radiogenic Sr_i.

Previous and new (this study) U–Pb studies of zircon from the magmatic belt reveal the presence of a small amount of older radiogenic Pb, essentially seen through the ^{235}U–^{207}Pb chronometer (Figs 3–5). Such inherited components reflect relict zircon extracted by the magmas from the melted source lithologies, present either in the subcontinental lithospheric mantle or in the overlying continental crust. In addition to zircon in kimberlites, the presence of old zircon in the lithospheric mantle has been demonstrated for plagiogranite dikes intruding the lithospheric peridotites of the European plate margin (Borsi *et al*., 1996). In either case, the ultimate source of inheritance is continental crust material, either integrated into the subcontinental mantle during ancient subduction or directly extracted from the overlying crust by the ascending mantle-derived magmas. Such inheritance is consistent with internal differences

in εHf_i, such as observed in two zircon populations extracted from a granodiorite and a micro-gabbro (Ab-138, -153, Fig. 6).

Further corroboration for the incorporation of different components is revealed by differences in Pb_i and Sr_i, in both plagioclase and clinopyroxene fractions from the same rock (samples Ab-133; -134; -135; -153; -157; Tables 4 and 5). This could reflect mixing of crystals from partly crystallized magmas or extraction of xenocrystic grains from the wall-rocks. Whatever explanation is preferred for these intra-rock isotope differences, it should be recognized that they are very small and therefore these contributions have not significantly changed the isotopic composition of the Oligo-Miocene magmas. This is well illustrated by the preservation of primary basaltic–gabbroic compositions even for those that show such isotopic heterogeneities.

Concerning potential crustal contamination of the parental mantle-derived magmas, none of our Pb_i values exceeds the reference field for subcontinental lithospheric mantle (Figs 7, 8, and 10a). The most sensitive tracer for continental material is Pb, for which 1–2% of crustal material would significantly shift the Pb_i signatures of the mantle-derived magmas (e.g. Schärer, 1991). Other isotope tracers such as Sr, Nd and Hf are more robust to crustal contamination. To further quantify potential crustal contamination, we have used Sr, which is the most sensitive crustal isotopic tracer after Pb. Crustal end-members can be estimated from the isotopic composition of Paleozoic granites and basement rocks of the region (33°S, Fig. 1; Parada *et al.*, 1999), yielding a $^{87}Sr/^{86}Sr$ of 0·7090 and a Sr concentration of 219 ppm. To estimate the mantle component, we used data for spinel-peridotite xenoliths found in Miocene volcanic rocks in Argentina that gave $^{87}Sr/^{86}Sr$ of 0·7038 and a Sr concentration of 22·3 ppm (Conceição *et al.*, 2005). In this case, 2% of a crustal melt would shift the initial $^{87}Sr/^{86}Sr$ of the mantle-derived magmas to 0·704, whereas 5% contamination would produce an initial Sr isotope ratio of 0·7066, reflecting the most radiogenic composition measured in our Oligo-Miocene samples. In most of our samples initial $^{87}Sr/^{86}Sr$ lies around 0·704–0·705 (Table 5), significantly less radiogenic than the value for 5% crustal components. If we used a more radiogenic crustal component in the model (e.g. $^{87}Sr/^{86}Sr = 0·714$), the potential crustal melt contributions would be much lower.

A further argument for a very small crustal component, or even its absence, is given by comparison of our Pb_i values with those of lower crustal rocks such as pyroxene–garnet granulites underlying the area (Kay *et al.*, 1996). In the α–β diagram, these granulite compositions plot outside the frame of Fig. 7a ($^{206}Pb/^{204}Pb$: 17·06–17·80), whereas they are included in the α–γ plot of Fig. 7b. In both cases these lower crust reference values are distinct from the initial isotopic signatures of the O-M belt, and such contamination cannot be seen. As mentioned above, the absence of any correlation between initial Nd isotope ratios and SiO_2 in these rocks also constrains crustal contamination to be insignificant (Kay *et al.*, 2005).

Initial hafnium isotope ratios indicate magma sources that are about 50% less depleted in LILE/HFSE than MORB sources (Fig. 6) and initial $^{87}Sr/^{86}Sr$ values are significantly more radiogenic (Table 5). A major difference is also observed for Th/U model ratios of the mantle source, which range from 3·9 to 4·1 (Table 4); these are higher than any value for Pacific MORB source mantle (Th/U = 3·7–3·8).

From a tectonic point of view it has been proposed that melts from asthenospheric mantle sources (i.e. melts from MORB-source mantle) provide the major component of the Oligo-Miocene magmas; however, neither our new or previous isotope data (Figs 7–11) are consistent with this hypothesis. As a consequence, the model of Kay *et al.* (2005) for the petrogenesis of the Oligo-Miocene magmas by decompression melting of the asthenoshere underneath extending continental lithosphere has to be questioned (e.g. Kay *et al.*, 2005). All the Pb_i, Sr_i, Hf_i, and Th/U signatures of the Oligo-Miocene magmatic rocks in central Chile are consistent with their derivation from subcontinental lithospheric mantle. It is therefore plausible that the parental magmas to rock types ranging from basalt–gabbro to rhyolite–granite are derived from slightly LILE/HFSE-depleted lithospheric mantle reservoirs with high U/Pb.

Using an average value of +8·0 for εHf_i (full range = +6·9 to +9·6; Table 6), a model age of 2·0 Ga is obtained for formation of the subcontinental mantle and corresponding continental crust. At 2 Ga, we assume that the difference between the depleted and primitive mantle was still small. Initial $^{87}Sr/^{86}Sr$ isotope ratios of the primitive mantle would have been 0·70123 (Rb/Sr = 0·027), and initial $^{206}Pb/^{204}Pb$ 12·685 (for $\mu = 7·13$) using the Rb/Sr and U/Pb ratios of the primitive mantle from Hofmann (1988) and Stacey & Kramers (1975). Because crust extraction around 2·0 Ga would necessarily cause Rb and U depletion in the residual mantle, the Rb/Sr at that time would have been around 0·017, and μ at about 5·3, yielding a present-day $^{87}Sr/^{86}Sr$ of 0·702 and a $^{206}Pb/^{204}Pb$ of 14·613. Both these model ratios are significantly lower than the initial isotope ratios determined for the Oligo-Miocene mantle sources. In consequence, the 2·0 Ga depleted mantle underneath the South American continent must have been re-enriched in Rb and U, most probably through metasomatism occurring in relation to ancient subduction events, previously suggested to explain the inherited zircon components. This metasomatized mantle would have evolved with an average model Rb/Sr of about 0·039, and a μ of about

16·3. It should be noted that both these ratios are similar to those measured in some garnet-peridotite xenoliths from South Africa (Kimberley) and the Canadian Arctic (Hawkesworth *et al.*, 1990; Schmidberger *et al.*, 2001). The 2·0 Ga Hf model age is consistent with a 2·1–1·8 Ga upper zircon intercept and Nd model ages obtained for Paleozoic and Cenozoic rocks in the central Andes (Franz *et al.*, 2006).

To induce Oligo-Miocene melting within the Andean metasomatized lithospheric mantle, the most plausible model is fluid release from the subducting Nazca–Farallon plate. Petrological data show that such melting occurred successively in the garnet and spinel stability fields (Nyström *et al.*, 2003), reflecting an increasing depth of melting from Oligocene to Miocene times. A crucial question is how the large variation of lithologies was produced. A first-order observation is that basalts (gabbros) and andesites (diorites) make up more than 90% of the magmatic rocks. The evolution from olivine-basalts to andesites may be explained by a combination of (1) original chemical differences in the metasomatized subcontinental mantle source, (2) differences in the degree of mantle melting, and (3) crystal fractionation in the garnet and spinel stability fields. To explain further chemical differentiation towards rhyolitic–granitic compositions, further fractional crystallization must have played a role, occurring during magma ascent beneath and within the plagioclase stability field. For the latter, this is indicated by the presence of Eu anomalies previously reported for some samples (Nyström *et al.*, 2003; Kay *et al.*, 2005).

CONCLUSIONS

(1) The new U–Pb zircon ages confirm a period of about 16 Myr of calc-alkaline magmatism in central Chile, from 28·1 to 11·5 Ma. Together with previous dating results from the same region, the full period of continuous magmatism seems to have occurred between 28·8 and 5·2 Ma.

(2) Fluid-induced magma generation from old metasomatized subcontinental lithospheric mantle satisfies all the isotope signatures of the magmatic products. These lithospheric mantle sources are characterized by weak to moderate LILE/HFSE depletion and high $^{238}U/^{204}Pb$. The Hf model age for major lithospheric mantle formation at about 2 Ga is in agreement with earlier model ages from the region.

(3) Genesis of basalts–gabbros and andesites–diorites constituting 90% of the magmatic belt seems to reflect a combination of (1) different degrees of partial melting of the mantle source, (2) original chemical (metasomatic) differences within the subcontinental mantle, and (3) crystal fractionation in both the spinel- and garnet-peridotite stability fields. The petrogenesis of the more evolved magmas (rhyolites–granites) most probably involves differentiation through fractional crystallization at mantle depths and within the crust, possibly inducing some very minor crustal melting.

ACKNOWLEDGMENTS

For technical assistance we thank J.-P. Goudour and M. Manetti, and we appreciated helpful advice during field work by A. Demant, E. Godoy, J. J. Verdugo, S. Calderon, F. C. Fuentes, J. Vargas and F. Rodriguez. For critical reading and helpful suggestions on earlier versions of the manuscript we are indebted to K. Deckart. Detailed reviews by S. Noble, T. Waight, G. Wörner and J. Gamble have helped to considerably improve the manuscript. For funding the project we thank FONDECYT (numbers 1020809 and 1061266) and ECOS-CONICYT (C03U01). P. Montecinos thanks CONICYT for providing a 3 years grant for his Ph.D. thesis.

REFERENCES

Aguirre, L. (1960). *Geología de los Andes de Chile central (provincia de Aconcagua). Instituto de Investigaciones Geológicas, Santiago, Boletín* **9**, 70 pp.

Aguirre, L., Robinson, D., Bevins, R. E., Morata, D., Vergara, M., Fonseca, E. & Carrasco, J. (2000). A low-grade metamorphic model for the Miocene volcanic sequences in the Andes of central Chile. *New Zealand Journal of Geology and Geophysics* **43**, 83–93.

Bach, W., Erzinger, J., Dosso, L., Bollinger, C., Bougault, H., Etoubleau, J. & Sauerwein, J. (1996). Unusually large Nb–Ta depletions in North Chile ridge basalts at 36°50′ to 38°56′S: major element, trace element, and isotopic data. *Earth and Planetary Science Letters* **142**, 223–240.

Beccar, I., Vergara, M. & Munizaga, F. (1986). Edades K–Ar de la Formación Farellones, en el cordón del cerro La Parva, Cordillera de los Andes de Santiago, Chile. *Revista Geológica de Chile* **28–29**, 109–113.

Ben Othman, D., White, W. M. & Patchett, J. (1989). The geochemistry of marine sediments, island arc magma genesis, and crust–mantle recycling. *Earth and Planetary Science Letters* **94**, 1–21.

Blichert-Toft, J. & Albarède, F. (1997). Lu–Hf isotope geochemistry of chrondrites and the evolution of mantle–crust system. *Earth and Planetary Science Letters* **148**, 243–258.

Blichert-Toft, J., Chauvel, C. & Albarède, F. (1997). Separation of Hf and Lu for high-precision isotope analysis of rock samples by magnetic sector–multiple collector ICP-MS. *Contributions to Mineralogy and Petrology* **127**, 248–260.

Bodet, F. & Schärer, U. (2000). Evolution of the SE-Asian continent from U–Pb and Hf isotopes in single grains of zircon and baddeleyite from large rivers. *Geochimica et Cosmochimica Acta* **64**, 2067–2091.

Borsi, L., Schärer, U., Gaggero, L. & Crispini, L. (1996). Age, origin and geodynamic significance of plagiogranites in lherzolites and gabbros of the Piedmont–Ligurian basin. *Earth and Planetary Science Letters* **140**, 227–241.

Charrier, R., Baeza, O., Elgueta, S., Flynn, J. J., Gans, P., Kay, S. M., Muñoz, N., Wyss, A. R. & Zurita, E. (2002). Evidence for Cenozoic extensional basin development and tectonic inversion south of the

flat-slab segment, southern Central Andes, Chile (33°–36°S.L.). *Journal of South American Earth Sciences* **15**, 117–139.

Chauvel, C. & Blichert-Toft, J. (2001). A hafnium isotope and trace element perspective on melting of the depleted mantle. *Earth and Planetary Science Letters* **190**, 137–151.

Conceição, R., Mallmann, G., Koester, E., Schilling, M., Bertotto, G. & Rodriguez-Vargas, A. (2005). Andean subduction related mantle xenoliths: isotopic evidence of Sr–Nd decoupling during metasomatism. *Lithos* **82**, 273–287.

Davies, G. R., Spriggs, A. J. & Nixon, P. H. (2001). A non-cognate origin for the Gibeon Kimberlite megacryst suite, Namibia: Implications for the origin of Namibian kimberlites. *Journal of Petrology* **42**, 159–172.

Deckart, K. & Godoy, E. (2006). Barren igneous intrusives in the Central Andes: U/Pb geochronology and Nd–Hf isotope geochemistry. In: *Extended Abstracts Volume, V, South American Symposium on Isotope Geology.* Montevideo: SSAGI (CD).

Deckart, K., Clark, A., Aguilar, C., Vargas, R., Bertens, A., Mortensen, J. & Fanning, M. (2005). Magmatic and hydrothermal chronology of the giant Rio Blanco Porphyry Copper Deposit, central Chile: Implications of an integrated U–Pb and $^{40}Ar/^{39}Ar$. *Economic Geology* **100**, 905–934.

DePaolo, D. J. & Wasserburg, G. J. (1976). Nd isotopic variations and petrogenetic models. *Geophysical Research Letters* **3**, 249–252.

Devey, C. W., Hémond, C. & Stoffers, P. (2000). Metasomatic reactions between carbonated plume melts and mantle harzburgite: the evidence from Friday and Domingo seamounts (Juan Fernandez chain, SE Pacific). *Contributions to Mineralogy and Petrology* **139**, 68–84.

Drake, R. E., Curtis, G. & Vergara, M. (1976). Potassium–argon dating of igneous activity in the Central Chilean Andes—latitude 33°S. *Journal of Volcanology and Geothermal Research* **1**, 285–295.

Franz, G., Lucassen, W., Trumbull, R., Romer, R. L., Wilke, H., Viramonte, J., Becchio, R. & Siebel, W. (2006). Crustal evolution at the Central Andean continental margin: a geochemical record of crustal growth, recycling and destruction. In: Oncken, O., Chong, G., Franz, G., Götze, H., Ramos, V., Strecker, M. & Wigger, P. (eds) *The Andes—Active Subduction Orogeny.* Berlin: Springer, pp. 45–64.

Fuentes, F., Vergara, M., Aguirre, L. & Féraud, G. (2002). Relaciones de contacto de unidades volcanicas terciarias de los Andes de Chile central (33°S): una reinterpretación sobre la base de dataciones $^{40}Ar/^{39}Ar$. *Revista Geológica de Chile* **29**(2), 207–225.

Gana, P. & Wall, R. (1997). Evidencias geocronológicas $^{40}Ar/^{39}Ar$ y K–Ar de un hiatus Cretácico superior–Eoceno en Chile central (33–33°30′S). *Revista Geológica de Chile* **24**, 145–163.

Gerlach, D. C., Hart, S. R., Morales, V. W. & Palacios, C. (1986). Mantle heterogeneity beneath the Nazca Plate: San Felix and Juan Fernandez islands. *Nature* **322**, 165–169.

Godoy, E., Yáñez, G. & Vera, E. (1999). Inversion of an Oligocene volcano-tectonic basin and uplifting of its superimposed Miocene magmatic arc in the Central Chilean Andes: First seismic and gravity evidence. *Tectonophysics* **306**, 217–236.

Hawkesworth, C. J., Erlank, A. J., Kempton, P. D. & Waters, F. G. (1990). Mantle metasomatism: isotope and trace element trends in xenoliths from Kimberley, South Africa. *Chemical Geology* **85**, 19–34.

Heaman, L. H. (1989). The nature of the subcontinental mantle from Sr–Nd–Pb isotopic studies on kimberlite perovskite. *Earth and Planetary Science Letters* **92**, 323–334.

Hofmann, A. W. (1988). Chemical differentiation of the Earth: the relationship between mantle, continental crust and oceanic crust. *Earth and Planetary Science Letters* **90**, 297–314.

Hoffstetter, R., Fuenzalida, H. & Cecioni, G. (1957). *Léxique stratigraphique international, 7, Amérique Latine, Chili–Chile.* Paris: Centre National de la Recherche Scientifique, 444 pp.

Holmes, A. (1946). An estimate of the age of the Earth. *Nature* **157**, 680–684.

Jaffey, H., Flynn, K. F., Glendenin, L. E., Bentley, W. C. & Essling, A. M. (1971). Precision measurements of half-lives and specific activities of ^{235}U and ^{238}U. *Physical Reviews* **C4**, 1889–1906.

Karsten, J. L., Klein, E. M. & Sherman, S. B. (1996). Subduction zone geochemical characteristics in ocean ridge basalts from the southern Chile Ridge: Implications of modern ridge subduction systems for the Archean. *Lithos* **37**, 143–161.

Kay, S. M., Orrell, S. & Abbruzzi, J. M. (1996). Zircon and whole-rock Nd–Pb isotopic evidence for a Grenville age and a Laurentian origin for the basement of the Precordillera in Argentina. *Journal of Geology* **104**, 637–648.

Kay, S. M., Godoy, E. & Kurtz, A. (2005). Episodic arc migration, crustal thickening, subduction erosion, and magmatism in the south–central Andes. *Geological Society of America Bulletin* **117**, 67–88.

Kramers, J. D., Roddick, J. C. M. & and Dawson, J. B. (1983). Trace element and isotope studies on veined, metasomatic and 'MARID' xenoliths from Bultfontein, South Africa. *Earth and Planetary Science Letters* **65**, 90–106.

Krogh, T. E. (1973). A low contamination method for hydrothermal decomposition of zircon and extraction of U and Pb for isotopic ages determination. *Geochimica et Cosmochimica Acta* **37**, 485–494.

Kurtz, A., Kay, S. M., Charrier, R. & Farrar, E. (1997). Geochronology of Miocene plutons and exhumation history of the El Teniente region, Central Chile (34°–35°S). *Revista Geológica de Chile* **24**, 75–90.

Le Bas, M. J., Le Maitre, R. W., Streckeisen, A. & Zanettin, B. (1986). A chemical classification of volcanic rocks based on the total alkali–silica diagram. *Journal of Petrology* **27**, 745–750.

Levi, B., Aguirre, L., Nyström, J. O., Padilla, H. & Vergara, M. (1989). Low-grade regional metamorphism in the Mesozoic–Cenozoic volcanic sequences of the Central Andes. *Journal of Metamorphic Geology* **7**, 487–495.

Lucassen, F., Franz, T. G., Viramonte, J., Romer, R. L., Dulski, P. & Lang, A. (2005). The late Cretaceous lithospheric mantle beneath the Central Andes: Evidence from phase equilibria and composition of mantle xenoliths. *Lithos* **82**, 379–406.

Ludwig, K. R. (2003). *Isoplot 3.0, a Geochronological Toolkit for Microsoft Excel. Berkeley Geochronology Center Special Publications* **4**, 74 pp.

Manhès, G., Minster, J. F. & Allègre, C. J. (1978). Comparative U–Th–Pb and Rb–Sr study of the Saint Séverin amphoterite: consequence for early Solar System chronology. *Earth and Planetary Science Letters* **39**, 14–24.

Munizaga, F. & Vicente, J. C. (1982). Acerca de la zonación plutónica y del volcanismo miocénico en los Andes de Aconcagua (Lat. 32–33°S): datos radiométricos K–Ar. *Revista Geológica de Chile* **16**, 3–21.

Muñoz, M., Fuentes, F., Vergara, M., Aguirre, L., Nyström, J., Féraud, G. & Demant, A. (2006). Abanico East Formation: petrology and geochemistry of volcanic rocks behind the Cenozoic arc front in the Andean Cordillera, central Chile (33°50′S). *Revista Geológica de Chile* **33**(1), 109–140.

Nowell, G. M., Pearson, D. G., Bell, D. R., Carlson, R. W., Smith, C. B., Kempton, P. D. & Noble, S. R. (2004). Hf isotope systematics of kimberlites and their megacrysts: new constraints on their source regions. *Journal of Petrology* **45**, 1583–1612.

Nyström, J. O., Vergara, M., Morata, D. & Levi, B. (2003). Tertiary volcanism during extension in the Andean foothills of central

Chile (33°15′–33°45′S). *Geological Society of America Bulletin* **115**, 1523–1537.

Parada, M., Nyström, J. O. & Levi, B. (1999). Multiple sources for the Coastal Batholith of central Chile (31–34°S): geochemical and Sr–Nd isotopic evidence and tectonic implications. *Lithos* **46**, 505–521.

Patchett, P. J. (1983). Importance of the Lu–Hf isotopic studies of planetary chronology and chemical evolution. *Geochimica et Cosmochimica Acta* **47**, 81–91.

Patchett, P. J. & Tatsumoto, M. (1980). A routine high-precision method for Lu–Hf isotope geochemistry and chronology. *Contributions to Mineralogy and Petrology* **75**, 263–267.

Patchett, P. J., Kouovo, O., Edge, C. E. & Tatsumoto, M. (1981). Evolution of continental crust and mantle heterogeneity: Evidence from Hf isotopes. *Contributions to Mineralogy and Petrology* **78**, 279–297.

Ramos, V. (2000). The Southern Central Andes. In: Cordani, U. G., Milani, E. J., Thomaz Filho, A. & Campos, D. A. (eds) *Tectonic Evolution of South America. Abstracts, 31st International Geologic Congress*. Rio de Janeiro: International Union of Geological Sciences (IUGS) pp. 561–604.

Rivano, S., Godoy, E., Vergara, M. & Villaroel, R. (1990). Redefinición de la Formación Farellones en la Cordillera de los Andes de Chile Central (32°–34°S). *Revista Geológica de Chile* **17**, 205–214.

Schärer, U. (1991). Rapid continental crust formation at 1·7 Ga from a reservoir with chondritic isotope signatures, eastern Labrador. *Earth and Planetary Science Letters* **102**, 110–133.

Schärer, U., Corfu, F. & Demaiffe, D. (1997). U–Pb and Lu–Hf isotopes in baddeleyite and zircon megacrysts from the Mbuji-Mayi kimberlite: Constraints on the subcontinental mantle. *Chemical Geology* **143**, 1–16.

Schmidberger, S. S., Simonetti, A. & Francis, D. (2001). Sr–Nd–Pb isotope systematics of mantle xenoliths from Somerset Island kimberlites: Evidence for lithosphere stratification beneath Arctic Canada. *Geochimica et Cosmochimica Acta* **65**, 4243–4255.

Sguigna, A. P., Larabee, A. J. & Waddington, J. C. (1982). The half-life of ^{176}Hf by γ–γ coincidence measurements. *Canadian Journal of Physics* **60**, 361–364.

Smith, C. B. (1983). Pb, Sr and Nd isotopic evidence for sources of southern African Cretaceous kimberlites. *Nature* **304**, 51–54.

Stacey, J. S. & Kramers, J. D. (1975). Approximation of terrestrial lead isotope evolution by a two-stage model. *Earth and Planetary Science Letters* **26**, 207–221.

Steiger, R. H. & Jäger, E. (1977). Subcommission on geochronology: convention on the use of decay constants in geo- and cosmochronology. *Earth and Planetary Science Letters* **36**, 359–362.

Tatsumoto, M., Knight, R. J. & Allègre, C. J. (1973). Time differences in the formation of meteorites as determined from the ratio of 207-lead to 206-lead. *Science* **180**, 1279–1283.

Vergara, M. & Drake, R. (1979). Edades K/Ar en secuencias volcánicas continentales postneocomianas de Chile Central; su depositación en cuencas intermontanas restringidas. *Revista de la Asociación Geológica Argentina* **34**, 42–52.

Vergara, M., Charrier, R., Munizaga, F., Rivano, S., Sepúlveda, P., Thiele, R. & Drake, R. (1988). Miocene volcanism in the central Chilean Andes. *Journal of South American Earth Sciences* **1**, 199–209.

Vergara, M., Morata, D., Hickey-Vargas, R., López-Escobar, L. & Beccar, I. (1999). Cenozoic tholeiitic volcanism in the Colbun area, Linares Precordillera, Central Chile. *Revista Geológica de Chile* **26**, 23–41.

Vervoort, J. D., Patchett, P. J., Gehrels, G. E. & Nutman, A. P. (1996). Constraints on early Earth differentiation from hafnium and neodymium isotopes. *Nature* **379**, 624–627.

Vervoort, J. D., Patchett, P. J., Blichet-Toft, J. & Albarède, F. (1999). Relationships between Lu–Hf and Sm–Nd isotopic systems in the global sedimentary system. *Earth and Planetary Science Letters* **168**, 79–99.

Weis, D. & Demaiffe, D. (1985). A depleted mantle source for kimberlites from Zaire: Nd, Sr and Pb isotopic evidence. *Earth and Planetary Science Letters* **73**, 269–277.

White, W. M., Patchett, J. & Ben Othman, D. (1986). Hf isotope ratios of marine sediments and Mn nodules: evidence for a mantle source of Hf in seawater. *Earth and Planetary Science Letters* **79**, 46–54.

Zartman, R. E. & Doe, B. R. (1981). Plumbotectonics—the model. *Tectonophysics* **75**, 135–162.

Appendix: Petrographic Description of Studied Samples

Sample	Rock type	Locality	UTM coordinates*		Petrographic observations
			N	E	
Ab-99	Olivine basalt	Juncal high	6358576	392112	Glomero-porphyritic texture containing 5–20% euhedral to subhedral olivine (1–2 mm) crystals. Augite crystals are 1–3 mm (2–5 vol.%,) and plagioclase 1–5 mm (10–40 vol.%). Originally intergranular groundmass is composed of very small grains (<0·2 mm) of plagioclase, clinopyroxene and minor olivine. A chlorite–epidote–calcite assemblage represents altered augite
Ab-77	Basalt	Juncal high	6357391	391886	Porphyritic texture containing 5–10 vol.% euhedral to subhedral olivine (1–2 mm) crystals. Augite crystals are 1–3 mm (~5 vol.%) and plagioclase 1–5 mm (~30–25 vol.%). Originally intergranular groundmass is composed of very small grains (<0·2 mm) of plagioclase, clinopyroxene and minor olivine
Ab-86	Basalt	Juncal high	6358251	390740	Porphyritic texture containing ~20% euhedral to subhedral olivine (1–2 mm) crystals. Augite crystals are 1–3 mm (~2 vol.%), and plagioclase 1–5 mm (~8 vol.%). Originally intergranular groundmass is composed of very small grains (<0·2 mm) of plagioclase, clinopyroxene and minor olivine
Ab-142	Gabbro sill	Polvareda	6354125	387000	Medium-grained rock composed of large fresh augite (1–2 mm) and rare pigeonite, <2% of olivine, and 30–50% of fresh 1–4 mm plagioclase. Apatite is an accessory mineral. Secondary minerals are calcite and chlorite in some augites, and phengite–sericite in most altered plagioclase crystals
Ab-154	Pyroxene andesite	Juncal high	6363055	392564	Clinopyroxene-carrying andesitic flow, characterized by glomero-porphyric texture. Composed of partially altered andesine, glomerocrysts of augite floating in a groundmass of altered glassy matrix. Micro-phenocrysts (<0·2 mm) of clinopyroxene and plagioclase also form the groundmass. Calcite, smectite and albite are secondary phases occurring in the most altered domains of the andesine phenocrysts. Epidote, calcite, and chlorite are secondary minerals formed after clinopyroxene
Ab-156	Pyroxene andesite	Portillo	6366029	395430	Clinopyroxene-carrying andesitic flow, characterized by glomero-porphyric texture. Composed of fresh to intensely altered andesine, glomerocrysts of augite floating in a groundmass of altered glassy matrix, locally showing pilotaxic plagioclase. Micro-phenocrysts (<0·2 mm) of clinopyroxene and plagioclase also form the groundmass. Calcite, smectite and albite are secondary phases occurring in the most altered domains of the andesine phenocrysts. Epidote, calcite, and chlorite are secondary minerals formed after clinopyroxene
Ab-159	Pyroxene andesite	Riecillos	6350030	374633	Clinopyroxene-carrying andesitic flow. Composed of fresh andesine, glomerocrysts of augite floating in a groundmass of altered glassy matrix. Micro-phenocrysts (<0·2 mm) of clinopyroxene and plagioclase also form the groundmass
Ab-133	Dacitic sill	Juncal high	6362515	392414	Porphyritic texture composed of plagioclase phenocrysts (~1·5 mm, 8 vol.%) and of fresh to partially altered muscovite (0·5–1·6 mm, 2 vol.%). Groundmass of fine-grained feldspar, minor quartz and muscovite. Secondary calcite and sericite are observed in strongly altered plagioclase. Accessory minerals are zircon and titanite
Ab-143	Dacitic sill	Polvareda	6352200	389150	Porphyritic texture composed of plagioclase phenocrysts (1·5–2 mm, 5 vol.%) and of fresh to partially altered muscovite (0·8–2 mm, 2 vol.%). Groundmass of fine-grained feldspar and minor quartz. Secondary calcite and sericite are observed in strongly altered plagioclase. Accessory minerals are zircon and titanite
Ab-152	Andesitic sill	Portillo	6366727	394060	Porphyritic texture composed of plagioclase phenocrysts (1·5–2 mm, 10 vol.%) and of fresh to partially altered amphibole (0·8–2 mm, 5 vol.%). Groundmass of fine-grained feldspar and minor quartz. Secondary calcite and sericite are observed in strongly altered plagioclase. Accessory minerals are apatite, zircon and titanite

(continued)

Appendix: Continued

Sample	Rock type	Locality	UTM coordinates*		Petrographic observations
			N	E	
Ab-45	Trachyandesite	Leones	6348576	387858	Clinopyroxene-carrying andesitic flow. Composed of fresh andesine, glomerocrysts of clinopyroxene floating in a groundmass of pilotaxic texture. Micro-phenocrysts (<0·2 mm) of altered pyroxene and fresh plagioclase also form the groundmass
Ab-47	Basaltic trachyandesite	Leones	6349488	386319	Porphyritic rock composed of intensely altered plagioclase (~2 mm, 50 vol.%), altered clinopyroxene floating in a groundmass of pilotaxic texture, minor olivine relicts. Micro-phenocrysts (<0·2 mm) of both altered pyroxene and plagioclase also form the groundmass
Ab-49	Basaltic trachyandesite	Leones	6349488	386319	Porphyritic rock composed of intensely altered plagioclase (~1 mm, 30 vol.%), altered clinopyroxene floating in a groundmass of pilotaxic texture, minor olivine relicts. Micro-phenocrysts (<0·2 mm) of both altered pyroxene and plagioclase also form the groundmass
Ab-53	Andesite	Blanco river	6350564	382655	Clinopyroxene-carrying andesitic flow. Composed of fresh andesine (30 vol.%) and glomerocrysts of clinopyroxene floating in a groundmass of intersertal texture. Micro-phenocrysts (<0·2 mm) of altered pyroxene and fresh plagioclase also form the groundmass. Apatite as accessory mineral
Ab-56	Trachyandesite	Blanco river	6344000	382795	Clinopyroxene-carrying andesitic flow. Composed of fresh andesine (20 vol.%), glomerocrysts of clinopyroxene floating in a groundmass of pilotaxic texture. Micro-phenocrysts (<0·2 mm) of altered pyroxene and fresh plagioclase also form the groundmass
Ab-110	Basaltic andesite	Riecillos	6355792	373347	Clinopyroxene-carrying lava flow, characterized by pilotaxic texture. Composed of fresh plagioclase phenocrysts (0·5–3 mm, 10 vol.%) and fresh augite phenocrysts (0·5–2 mm, 5 vol.%). Groundmass composed for micro-phenocrysts of plagioclase and pyroxene. Apatite as accessory mineral
Ab-157	Gabbro	Leones	6349827	384342	Medium-grained stock of poikilitic texture composed of fresh plagioclase (80 vol.%) and interstitial fresh to partially altered augite (~20 vol.%). Chlorite is the main secondary mineral. Zircon as accessory mineral
Ab-153	Micro-gabbro	Riecillos	6356835	375644	Fine-grained stock of poikilitic texture composed of fresh plagioclase (70 vol.%) and interstitial fresh to partially altered augite (~30 vol.%). Chlorite is the main secondary mineral. Zircon as accessory mineral
Ab-139	Andesitic hornfels	Riecillos	6350174	374708	Tremolite-andesite hornfels characterized by a fine-grained granoblastic texture, composed of tremolite, biotite and primary andesine. These contact metamorphic rocks are fresh, showing some minor epidote, sericite, chlorite and pumpellyite in rare altered domains
Ab-138	Granodiorite	Riecillos	6348212	373800	Medium-grained granodioritic stock. Composed of euhedral fresh plagioclase (1–3 mm, 50 vol.%), anhedral quartz (10 vol.%), orthoclase (5 vol.%), and intensely altered amphibole (15 vol.%). Sphene, magmatic epidote and zircon as accessory minerals
Ab-136	Diorite	Blanco river	6340466	383209	Fine-grained dioritic stock composed of fresh plagioclase (0·5–1 mm, 80 vol.%), clinopyroxene (0·5–1 mm, ~20 vol.%) and minor altered orthopyroxene. Zircon as accessory mineral
Ab-135	Granodiorite	Blanco river	6392380	383025	Medium-grained granodioritic stock. Composed of euhedral fresh plagioclase (1–3 mm, 40 vol.%), anhedral quartz (10 vol.%), orthoclase (5 vol.%), intensely altered biotite (15 vol.%) and amphibole (5 vol.%). Sphene and zircon as accessory minerals
Ab-134	Diorite	Juncal river	6365947	395345	Medium-grained diorite composed of fresh euhedral plagioclase (0·5–3 mm, 80 vol.%), clinopyroxene (15 vol.%) and minor altered orthopyroxene. Zircon as accessory mineral
Ab-132	Granodiorite	Portillo	6364927	394046	Granodioritic stock of porphyritic texture. Composed of fresh plagioclase (1–5 mm, 45 vol.%), fresh biotite (10 vol.%), fresh amphibole (0·5–3 mm, 5 vol.%), quartz (8 vol.%) and K-feldspar (~0·5 mm, 2 vol.%). Microcrystalline groundmass composed by plagioclase and minor quartz. Apatite and zircon as accessory minerals